TOPICAL REVIEW

Disordering phenomena in superionic conductors

David A Keen

Physics Department, Oxford University, Clarendon Laboratory, Parks Road,
Oxford OX1 3PU, UK
and
ISIS Facility, Rutherford Appleton Laboratory, Chilton, Didcot, Oxon OX11 0QX, UK

E-mail: d.a.keen@rl.ac.uk

Abstract
Superionic conductors are materials which exhibit exceptionally high ionic
conductivity whilst in the solid state. The manner in which certain
structures accommodate superionic conduction has preoccupied many scientists
throughout the latter part of the last century, beginning with the early debate
about the disordered structure of the superionic α-phase of silver iodide. In
this review, the key methods that have been used to deduce structural disorder
in superionic conductors are described, and the important results summarized.
The review focuses on simple archetypal systems, since these have dominated
the literature, concentrating on more recent work and including emerging
methodologies for deducing structural disorder. In most cases, the interpretation
of diffuse scattering, as observed in scattering measurements, has played a
crucial role in the understanding of these highly disordered systems and this is
considered in some detail.

(Some figures in this article are in colour only in the electronic version)

Contents

1. Introduction

1.1. Superionic behaviour

Superionic conductors are those materials that allow the macroscopic movement of ions through their structure, leading to exceptionally high (liquid-like) values of ionic conductivity whilst in the solid state. This behaviour typically occurs at elevated temperatures and is characterized by the rapid diffusion of a significant fraction of one of the constituent species within an essentially rigid framework formed by the other species. Superionic conductors are not merely scientific curiosities, since compounds with high ionic conductivities have a number of technological applications ranging from miniature, lightweight high-power-density lithium-ion batteries for heart pacemakers, mobile phones and laptop computers to high-capacity energy storage devices for next-generation 'clean' electric vehicles. For the purposes of this review, however, I shall restrict myself to describing the structural implications of superionic conduction, focusing on three key areas. These are summarized as follows:

(a) The characteristics of structures which facilitate ion mobility.
(b) The modification to, or disorder induced in, the structure as a result of ion motion.
(c) The main methods that have been used to elucidate the processes that give rise to disorder.

Of these, the latter two will be covered in greatest detail. The two main approaches which underlie investigations of disorder in crystalline materials result from the perception of the disorder under question—is the disorder a small deviation from the average crystalline lattice, or is the lattice surrounded by extensive structural disorder? For superionic materials, the former results in descriptions in terms of isolated defects and the latter gives rise to interpretations based on, for example, sublattice melting. Equally, superionic materials are extremely useful systems for testing new approaches for understanding structural disorder. This is because the disorder is often thermally activated; it can result from either a gradual or a first-order structural phase transition; the disorder may effect substantially different proportions of ions and the disorder may exist in one, two or three dimensions. There is therefore also a large amount of work, particularly in the cubic-stabilized zirconias, where characterizing low-temperature static defects is as important as understanding how the structure accommodates the observed high-temperature superionic conduction.

There does not appear to be a hard and fast definition of whether a given material is superionic or not. It is however generally accepted that the superionic label may be applied to a material whose ionic conduction is above $\sigma \sim 10^{-2}$ Ω^{-1} cm^{-1}, with the best superionic conductors achieving conductivities of $\sigma \sim 1$ Ω^{-1} cm^{-1} or better. One of the most interesting

structural aspects of the superionic process concerns how the disorder develops as the ionic conductivity increases. A material that has a superionic high-temperature phase may begin as an insulator at low temperature and the conductivity could change by many orders of magnitude before reaching the superionic state.

The manner in which the superionic state is achieved has been proposed [1] as a means to classify superionic materials, namely:

- Type I superionic materials become superionic at temperatures above a first-order structural phase transition. This behaviour is typified by the superionic α-phase of AgI. In this material the ionic conductivity increases by around three orders of magnitude, on passing through the β–α phase transition at 420 K.
- Type II superionic materials attain high levels of ionic conductivity following a gradual and continuous disordering process within the same phase. Below the superionic transition, T_c, the number of conducting defects increases rapidly before saturating above T_c. The superionic transition is often accompanied by an anomaly in the specific heat and lattice expansion. β-PbF$_2$ displays typical type II superionic behaviour.
- Type III superionic materials do not have a clear phase transition, but achieve high levels of ionic conduction via increased mobility of a (generally fixed) number of thermally activated defects. An Arrhenius plot of the temperature dependence of the ionic conductivity for a type III superionic conductor would show linear behaviour. Sodium β-aluminas are typical type III superionic materials.
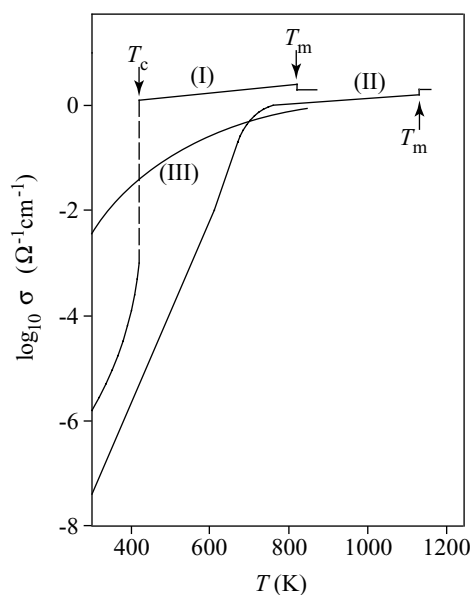
Typical plots of conductivity against temperature for three different types of superionic behaviour are shown in figure 1. This is a useful classification and it will be referred to throughout this review. However, when considering the disordering processes it actually makes more sense to organize the review by following the different structure types that display superionic conductivity. This is because a specific structure will often lend itself to a characteristic superionic behaviour.

1.2. Review outline

The outline of the rest of this review is as follows. First, there is a discussion of the important general structural considerations and the techniques that have been applied to unravel the structural complexity associated with superionic conduction. This includes both experimental and computational methods and is illustrated with examples where helpful. This is followed by a survey of superionic systems that are still being actively investigated. Wherever possible, recent work is used as examples, mostly restricted to that which is at most 15 years old. This should ensure that the review is genuinely topical—for discussion of the earlier work in this area, the reader is referred to reviews of the period [2–4].

2. General structural considerations

The general principles for effective superionic conduction are straightforward. First, it must be possible for the mobile ion to move between lattice sites. This usually means that a smaller ion will move through the 'static' sublattice of larger ions. Superionic conductors therefore tend to involve small cations such as Ag$^+$, Cu$^+$, Li$^+$, H$^+$, although larger highly polarizable anions may also give rise to significant ionic conductivity (e.g. F$^-$ or O^{2-}). Secondly, the ion movement must be macroscopic. The structure must have a fully connected network of lattice sites accessible to the mobile ions with low energy barriers between them. Thirdly, the mobility is enhanced if there are more sites for the conducting ion than there are ions to fill them, thus

Figure 1. A schematic plot of ionic conductivity against temperature for AgI (type I), β-PbF$_2$ (type II) and K β-alumina (type III). T_c and T_m mark the temperatures of the superionic and melting transitions, respectively.

reducing the effect of ions blocking other ions. This is facilitated either by a structure with an inherently large number of sites per mobile ion (such as α-AgI, whose structure possesses six tetrahedral sites per mobile cation), or by the formation of interstitial defects (e.g. β-PbF$_2$, whereby mobile anions move between sites via voids within the fluorite structure).

2.1. The time-average structure

2.1.1. Conventional interpretation of Bragg diffraction. The analysis of Bragg diffraction, whether from powdered or single-crystal samples, from x-ray or neutron diffraction, is the starting point for all structural investigations of crystalline superionic conductors. Bragg diffraction is strictly elastic scattering and the structure thus produced is a time-average structure. Average lattice sites are located and disorder may be inferred using a number of methods designed to mimic the deviation of the ion distribution from the average sites. The simplest of these are 'split-site' models. Here a single, occupied lattice site may be separated into a small number of nearby sites with proportionately reduced occupancy. These sites are often too close to each other to be simultaneously occupied. For example, in face-centred cubic (fcc) α-CuI, the four cations are located randomly within the eight tetrahedral 8(c) sites at $(\frac{1}{4}\frac{1}{4}\frac{1}{4})$ etc, within space group $Fm\bar{3}m$, each 50% occupied on average. There is evidence that the cation distribution about these sites is elongated in $\langle 111 \rangle$ directions away from the nearest anions. Hence a better fit to the Bragg diffraction data may be obtained by splitting each of the 8(c) sites into four sites at 32(f) at (xxx) etc, with $x \gtrsim 1/4$ and each $\frac{1}{8}$th occupied on average [5].

Another method that is often employed is to characterize the disorder using anisotropic temperature factors (or anisotropic atomic displacement parameters). These may be used independently, or in conjunction with split-site models. Here the deviations from the average lattice site are mimicked by a thermal ellipsoid that may elongate in certain directions to imply preferred directions for movement. This is especially true for systems that have one- or

two-dimensional conduction channels, when the thermal ellipsoids elongate in the directions permitted by the channels. Average structures of the one-dimensional superionic conductors based on hollandite are often characterized in this way [6].

A third method is to expand the temperature factors using terms based on an anharmonic model of the thermal motion. This can result in a large number of additional model parameters (see for example the anharmonic model for β-AgI [7]) and care must be taken to ensure that the data are sufficient to justify such a complicated model description.

The three methods described above all aim to describe the density distribution of mobile ions about their lattice sites more accurately than a simple lattice site model with isotropic temperature factors. The fundamental difficulty in doing this is that the Bragg scattering is elastic and so the data are not very sensitive to small deviations from the average structure. Locally correlated effects, which are often involved around defect formation, are not seen directly in the average structure. Another problem arises as a result of the paucity of the data, as alluded to in the previous paragraph. High-temperature disordered materials often do not show large numbers of Bragg peaks (for example, powder and single-crystal diffraction measurements of the superionic fcc phase of Li_2SO_4 observed four and twenty Bragg reflections, respectively [8, 9]). Therefore, great care must be taken to ensure that the data are not being overinterpreted using models with an inappropriately large number of structural parameters. As a general rule, the most reliable average structural models fit the data well with the smallest number of structural parameters possible, ideally with significantly fewer parameters than there are observed Bragg peaks.

2.1.2. The maximum-entropy Fourier difference method. More recently, the maximum-entropy (MaxEnt) Fourier difference method has been applied to superionic materials [10]. This technique [11] determines the most probable average distribution of the conducting ions within the unit cell, using the extracted peak intensities from a powder diffraction pattern in a statistically rigorous manner. The contribution of the 'known' parts of the structure to the scattering (i.e. the amplitudes and phases of the non-conducting sublattice) may also be included, as well as prior knowledge of the local smoothness and positivity (where applicable) of the scattering density distribution. As such, the method is less prone to excessive termination ripples that are an inevitable consequence of 'normal' Fourier methods. This method provides independent confirmation of the reliability of average structure models proposed using other techniques and may indeed also give indications of probable conduction pathways (see, for example, section 5.2.5b and [10]).

2.1.3. The bond valence summation method. The bond valence method has been used to check the plausibility of crystal structures for some time (see, for example [12]). The idea is very straightforward [13]. The total bond valence sum, V, of atom Y may be described in terms of its local environment, i.e.

$$V(Y) = \sum_i s_{Y-X_i}, \tag{1}$$

where X_i are the atoms near to atom Y and s_{Y-X_i} are the individual bond valences of bonds between atoms Y and X_i. s_{Y-X_i} are calculated from empirically determined tabulated bond valence parameters R_{Y-X} and b (e.g. [12]) and the observed bond length R_0:

$$s_{Y-X} = \exp\left(\frac{R_0 - R_{Y-X}}{b}\right). \tag{2}$$

To a good approximation, b is a universal constant, $b = 0.37$ Å [14]. Equilibrium sites within a crystal structure would be expected to correspond to values of V which are close to the

ideal valence for that particular atom. This has been further developed to investigate likely ion conduction pathways, by calculating the bond valence mismatch $\Delta V = |V - V_{ideal}|$ for the conducting ion throughout the structure and including the use of more advanced formulations of the bond valence sum [15, 16]. The most favourable pathway would correspond to the regions of the structure where ΔV is lowest. This has been used to good effect for a number of crystalline and amorphous systems (see e.g. [17] and section 5.2.5b).

2.2. Local structural environments

Having deduced the best average structure, it is now important to investigate it further, in order to understand the microscopic mechanism responsible for macroscopic superionic conduction. The first task would be to identify possible pathways within the structure that would provide an easy way for the conducting ion to pass through the structure. In some systems this is straightforward, for example the connected tetrahedral sites in the α-AgI structure, or the open layers in the two-dimensional β-aluminas. The MaxEnt Fourier difference method or bond valence summations described above (sections 2.1.2 and 2.1.3, respectively) may also provide strong indications of likely conduction pathways. For some other systems it is less obvious, especially for those which rely on defect ions for their conducting properties. An example of this would be the high-pressure rock-salt phase of AgI, which becomes a superionic conductor at high temperature when the silver ions move from the octahedral sites and into tetrahedral interstitials [18]. This produces a connected pathway of partially occupied tetrahedral $\leftrightarrow$ octahedral $\leftrightarrow$ tetrahedral sites in the fcc structure.

A second aspect is to investigate whether there are any distortions or relaxations of the lattice about the diffusing ions. This should not be unexpected, particularly since the diffusing ions may be residing, even if transiently, on sites which are unoccupied in the low-temperature stable structure. Considerable work in this area has been carried out in studies of the fluorite structured superionic conductors, particularly since different characteristic defects are found at different temperatures. This work is summarized in section 5.1. Related to this, it is important to investigate how the mobile ion is located within interstices. The interstitial sites may have a different symmetry from that which is more usually associated with the mobile ion and it is possible that, although it is found within the interstitial *void*, it does not reside centrally on the interstitial *site*. This can have implications for the conduction mechanism and an example of this is contained in section 5.2.2, which discusses recent work on the high-temperature structural behaviour of CuI.

Probably the key measurement for these local structural studies is diffuse scattering. This is the scattering observed in an x-ray or neutron diffraction experiment that is not Bragg scattering or from sources of background. It arises from local deviations of the structure from its time average and is often characterized by weak, broad features in the scattering pattern. Diffuse scattering, as outlined in section 3.1, may therefore be used to characterize the local changes in the structure as a result of the superionic conduction process. Other measurement techniques are also employed to determine the local structural environment of the conducting ions, notably the spectroscopic technique 'extended x-ray absorption fine structure' (EXAFS) and its contribution will be discussed in section 3.3. In addition, all these approaches have benefited from computer modelling, whether molecular dynamics (MD), Monte Carlo (MC) or reverse Monte Carlo (RMC) (see section 4). These methods have become more prominent in recent times, partly because of the difficulty of using analytical approaches for systems which are not highly ordered or completely disordered, but also because of the increases in accessible computer resources.

3. Local structural probes
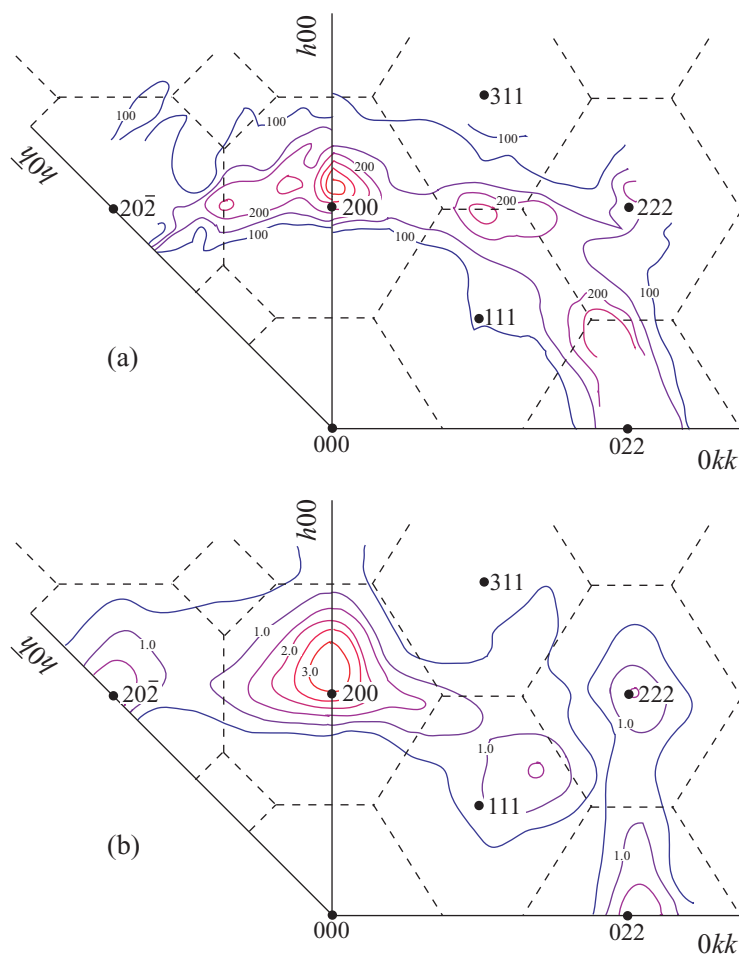
3.1. Diffuse scattering

Diffuse scattering in a scattering experiment may be loosely referred to as the scattering from the sample which is not Bragg scattering. As such it can have many origins, arising from, for example, lattice vibrations, stacking faults, substitutional, orientational or magnetic disorder in the material [19]. Of more relevance to superionic conductors, diffuse scattering may also arise from mobile ions or from lattice relaxation around defects associated with the conduction process. In a routine Bragg diffraction measurement it may be seen as an inconvenience, adding to the background signal and impeding the Bragg intensity extraction. However, it is a key signature for disordered structures and, when interpreted carefully, can be used to understand the form of disorder present in the material. For structural investigations, there are two basic measurements, the diffraction measurement and the elastic measurement.

3.1.1. Elastic diffuse neutron scattering. In the early days of diffuse scattering studies of the disordered structural features of superionic conductors, this was the method of choice. The two basic instruments for diffuse scattering studies were the triple-axis spectrometer [20] and the time-of-flight or 'chopper' spectrometer [21], both of which allow the separation of the elastically and inelastically scattered neutrons. Of these, triple-axis spectrometers were more commonly used for diffuse scattering from superionic materials, largely because those studying superionic conductors had easy access to such instrumentation at the neutron research reactors at Harwell, UK, and the Institut Laue-Langevin, France. The experimental method is straightforward; a large single crystal is placed on a neutron triple-axis spectrometer, configured to collect data corresponding to scattering events that do not change the energy of the neutron (within a certain energy resolution). A point-by-point grid of data is collected over a given reciprocal-lattice plane within the kinematic limits of the spectrometer. The data can be readily normalized using the expected intensities of phonon scattering. Using this experimental method, diffuse scattering that is inelastic in origin is minimized experimentally. This is very important when investigating elastic features near Bragg peaks, where acoustic phonon scattering (giving rise to strong thermal diffuse scattering) can be very intense at low energy transfers. In addition, an experimental distinction may be made between truly *elastic* coherent diffuse scattering (arising from static defects in the structure) and *quasielastic* coherent diffuse scattering (arising from defects in the structure which possess a finite lifetime). The former scattering is a delta function at zero neutron energy transfer, i.e. $\Delta E = 0$, and the latter scattering is centred on $\Delta E = 0$, but with a finite distribution in neutron energy transfer.

Figure 2(a) shows the energy-integrated quasielastic neutron scattering data from the fluorite, CaF_2, within its superionic region at 1473 K [22]. Here the quasielastic scattering was determined by measuring as a function of energy transfer across the elastic line at each Q-point using a triple-axis spectrometer and fitting a Lorentzian energy lineshape to the scattering profile. This quasielastic signal arises from deviations from the average structure and the integrated intensities as a function of scattering vector, Q, are used to determine possible defect cluster models and the linewidths are related to the likely lifetime of the defects.

The interpretation of elastic diffuse scattering from superionic conductors has been based on 'aggregated defect cluster' models [22–24] or 'correlated microdomains' [25]. The two methods are similar and use a formalism whereby a cluster is composed of vacancies, interstitials and relaxed ions. Vacancies are lattice sites that are not occupied within the cluster, interstitials are occupied non-lattice sites and relaxed ions occupy non-lattice sites close to the lattice site that they would occupy in the regular, defect-free, lattice. The diffuse scattering is

Figure 2. (a) Integrated quasielastic coherent diffuse scattering from a single crystal of CaF_2 measured using a triple-axis neutron spectrometer (after [22]). The right- and left-hand sides of the $h00$ axis correspond to data in the $01\bar{1}$ reciprocal-lattice plane at 1475 K and difference data (1475–1273 K) in the 010 reciprocal-lattice plane, respectively. (b) Equivalent reciprocal-lattice planes of diffuse scattering from CaF_2 calculated using a defect cluster composed of nine vacancies that arise from one 'true' anion interstitial and eight relaxed anions (see [22] for details).

then calculated for the defects by assuming that they are isolated and non-interacting or that they aggregate in prescribed ways (see [22–25] for details).

3.1.2. Diffuse scattering in x-ray and neutron diffraction. These types of experiments are usually designed to survey large volumes of reciprocal space rapidly, normally using single-crystal samples. The simplest, and certainly the earliest, is the Laue x-ray photograph [26]. Other photographic x-ray methods using monochromatic x-ray beams are also popular [27]. More recently, two-dimensional image plates or CCDs have been used instead of film [28, 29]. These methods all cover a wide area of reciprocal space in a single exposure and show regions of strong diffuse scattering very rapidly. Other quantitative x-ray methods use position-sensitive detectors instead of film, or even single detectors with analysers, and result in high-
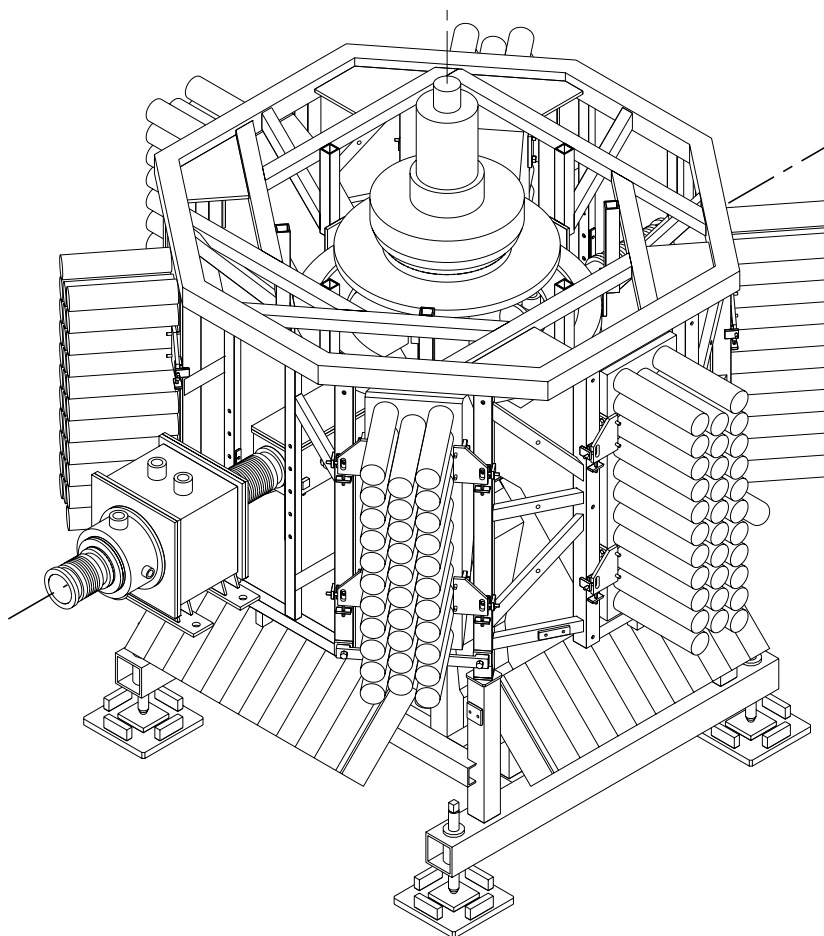
Figure 3. A diagram showing the 11-detector array on the neutron time-of-flight SXD. Each position-sensitive detector consists of a 64×64 array of 3×3 mm^2 pixels. The instrument is designed with six detectors in the equatorial plane and five below the equatorial plane forming a cross underneath the sample. Around 50% of the scattering from the single crystal is collected by the detectors, with almost uninterrupted coverage both in the equatorial plane over a wide range of 2θ scattering angle and around the sample at $2\theta = 90°$.

quality data [30, 31]. In contrast, neutron diffraction techniques have not traditionally been used for diffuse scattering surveys. However, new instrumentation such as the time-of-flight single-crystal diffractometer, SXD, at the ISIS spallation neutron source, has been used very successfully [32]. Here the combination of a large array of two-dimensional, position-sensitive detectors (see figure 3) and a time-sorted polychromatic neutron beam allows extremely large volumes of reciprocal space to be collected for each crystal position.

3.2. Total scattering

A total scattering measurement aims to measure all the scattering from a (usually powdered) sample (Bragg and diffuse scattering, elastic and inelastic scattering) in a manner that can be rigorously corrected [33, 34] to yield the so-called 'total scattering structure factor', $i(Q)$,

which contains the interference terms from the total scattering cross-section [35]. This may then be Fourier transformed to give a total pair correlation function, $D(r)$, which in turn may be used to determine the instantaneous atom–atom correlations in a material. Formally, the scattering from a polycrystalline sample with n distinct species, j, each in proportion c_j, per atom N, may be defined as

$$\frac{1}{N}\frac{\mathrm{d}\sigma}{\mathrm{d}\Omega} = i(Q) + \sum_{j=1}^{n} c_j \overline{b_j^2}, \tag{3}$$

where $4\pi \sum_{j=1}^{n} c_j \overline{b_j^2}$ is the Q-independent total scattering cross-section of the material and $i(Q)$ is the total scattering structure factor. This may be Fourier transformed to yield a total pair distribution function, $D(r)$:

$$D(r) = \frac{2}{\pi} \int_0^{\infty} Q i(Q) \sin(Qr)\,\mathrm{d}Q, \tag{4}$$

which in turn is composed of a weighted sum of partial pair correlation functions $g_{ij}(r)$:

$$D(r) = 4\pi r \rho_0 \sum_{i,j=1}^{n} c_i c_j \bar{b}_i \bar{b}_j [g_{ij}(r) - 1]. \tag{5}$$

Here ρ_0 is the number density of the material and $\bar{b}_j$ is the neutron scattering length of species j. Similar formalisms exist for x-ray total scattering, although they are more complex, due to the Q-dependent x-ray scattering form factor. Other related functions have also been defined in the literature, such as $F(Q)$, $S(Q)$, $T(r)$ and $G(r)$, and their interrelationship has been detailed previously [35]. The information contained in total scattering is fundamentally different from the time-averaged structure obtained from an elastic measurement, since it corresponds to a 'snapshot' in time of the structure. This means that models produced using total scattering data will also represent the structure at an instant of time and any ions undergoing motion will appear 'frozen'.

These measurements, applied to superionic conductors, have come to the fore in recent years as a result of improved instrumentation (particularly time-of-flight neutron diffraction) and developments of modelling methods such as the RMC technique (see section 4.3). Also, there has been an increased interest in the relationship between the structures of the disordered crystal (just below the melting temperature, T_M) and the molten salt (above T_M) [36]. Total scattering measurements taken above and below T_M allow a direct comparison of the crystalline and molten local structures (see, for example, figure 4).

3.3. EXAFS

EXAFS measures the interference pattern between a photoelectron excited from the core level of an atom and the potential generated by the surrounding atoms. It is therefore an atom-selective local structure probe that can be used to determine the local environment of specific elements in a material. A very good review of the subject, focusing on liquid studies but applicable to other disordered systems, has recently been published [37]. This, taken together with a recent theoretical review [38] gives a very good summary of the current state of EXAFS spectroscopy and methods for its interpretation. The structural information gained from an EXAFS experiment is similar to that obtained from total scattering in so far as it is sensitive to the instantaneous positions of atoms and average atom locations can only be inferred from the data. Radial distribution functions, obtained from EXAFS data, are dominated by short-range correlations (since the photoelectron has a short lifetime, or mean free path, in the material) and the limited range of data in reciprocal space can broaden the real-space peaks. The ability
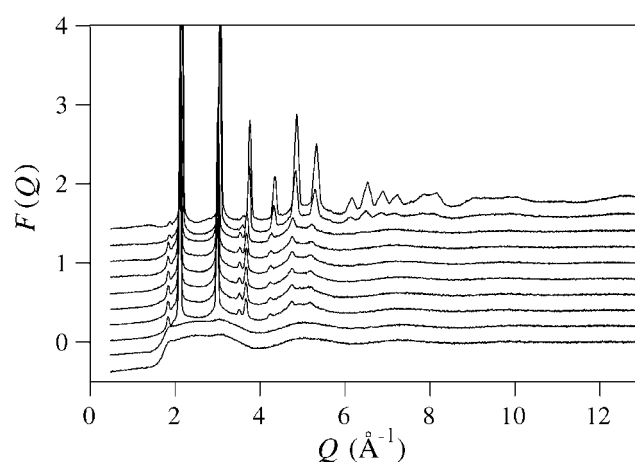
Figure 4. Neutron total scattering from powdered AgBr at (from top to bottom) 293 K (offset vertically by 1.8), 490, 669, 684, 689, 697, 698, 699, 703 and 706 K. Each successive plot is offset vertically by -0.2. There is a strong similarity between the diffuse scattering in the total scattering from crystalline AgBr just below melting ($T_M = 701$ K) and the total scattering from molten AgBr (after [48]).

to probe the environment of a specific atom is a big advantage, particularly for doped systems. Another advantage over total scattering methods is that EXAFS, at least in principle, is sensitive to many-atom correlations in the system.

EXAFS, with a few notable exceptions, has not been used extensively on superionic conductors. Initially this was probably due to uncertainties in the interpretation of the EXAFS signal and even now, with a much-improved theoretical characterization of EXAFS, it can be difficult to extract precise information about mobile ions within a crystalline material from EXAFS. One early exception to this is the work on AgI, CuI, CuCl and CuBr (see [39] and references therein). Here EXAFS results were used to develop an excluded-volume model for superionic conduction [40] and as a method for determining nearest-neighbour interaction potentials [41]. Other more recent examples include further EXAFS measurements on AgBr and on superionic glasses. Both will be covered in later sections of this review (see sections 5.2.3 and 5.4, respectively).

4. Computer modelling

Computer modelling has proved a popular way to understand the disorder associated with superionic conduction. This is for a number of reasons. First, by definition, the disorder is dynamic in origin. This means that more established methods for understanding diffuse scattering, such as those which use analytical expansions of the scattering equations, attributing the different terms to specific structural features, are not particularly effective. (Although these methods do work at low temperatures in cases where the disorder arises from doping and the static disorder around the dopant ion is being investigated.) Secondly, in many cases, the disorder is extensive. Computer simulation has played an important role in the development of structural models of liquids and can also be applied to amorphous or 'liquid-like' crystalline superionic materials. Thirdly, and most pragmatically, the subject has come to the fore with the advent of better and better computers. Superionic conductors have been used to demonstrate the effectiveness of these simulation techniques. The most successful method has probably

been MD simulation, since the simulations can be used to not only produce a disordered structure but also the dynamics associated with ionic conduction. The MC-based methods (MC and RMC) will yield the structure, and although MC simulation may be used to determine thermodynamical properties, it has rarely been used to investigate superionic conductors in such a rigorous manner. In this section we will consider briefly the three methods in turn, and refer to later sections where they have been used effectively.

4.1. Molecular dynamics simulation

The concept behind MD simulation is very straightforward. Atoms within a configuration, with positions, $x(t)$, and velocities, $v(t)$, at time, t, are moved to positions, $x(t + \Delta t)$, and velocities, $v(t + \Delta t)$, at time $t + \Delta t$, on the basis of given interatomic potentials and Newton's laws of motion. The method relies on the approximation that for small Δt, the acceleration on any given particle is constant for the whole time step, Δt. This is only true in the limit $\Delta t \rightarrow 0$ and various algorithms have been proposed to provide a good approximation to the exact solution whilst still retaining a computationally sensible value of Δt [42].

It can be quickly appreciated that MD simulation is a very useful method for investigating superionic conductors (see, for example, [43]). The atom positions may be used to extract structural parameters (average positions and instantaneous correlations) and atom trajectories may be traced to investigate diffusion pathways and mechanisms. In addition, since the velocities are recorded at each time step, dynamical processes may also be extracted, such as lattice vibrations and phonon density of states. The main drawback of the method is that it is more computationally costly than the MC-based methods. This tends to mean that smaller configurations of atoms must be used for MD simulation.

4.1.1. The RVP potential. Many MD studies of copper- and silver-based superionic materials have used the so-called RVP two-body effective interatomic potential, named after the three workers who developed it [44, 45]. The two-body potential is formulated in the following manner:

$$V_{ij}(r) = \frac{A_{ij}(\sigma_i + \sigma_j)^{n(ij)}}{r^{n(ij)}} + \frac{Z_i Z_j e^2}{r} - \frac{1}{2}(\alpha_i Z_i^2 + \alpha_j Z_j^2)\frac{e^2}{r^4} - \frac{W_{ij}}{r^6}$$

(6)

$$(a) \qquad\qquad (b) \qquad\qquad (c) \qquad\qquad (d)$$

where (a) is an r^{-n} core repulsion term which approximates $\exp(-r/\rho)$ behaviour; (b) is a point charge electrostatic term; (c) is a polarization term describing the secondary interaction between the ion and the polarization that it induces on a neighbouring ion; and (d) is the first term in a polynomial expansion characterizing the van der Waals interaction which describes the simultaneous polarization of the two ions' electron distributions. A_{ij}, α_i and W_{ij} are constants, σ_i are ionic radii and Z_i are effective ionic charges. This potential has been very successful in describing (amongst others) the disorder in AgI, CuI (section 5.2.2) and Ag_2Se (section 5.2.4) and the sequence of phase transitions in AgI as a function of pressure and temperature [46].

4.2. Monte Carlo simulation

MC simulations also use a set of interaction potentials. These are used to calculate the energy, E, of a configuration of atoms. The method of importance sampling, first suggested by Metropolis *et al* [47], is used to determine the probability of the configuration changing between

two states. In essence this means that the configuration is allowed to change between two states depending on the change in energy of the two states. A common probability function is given by

$$P = \begin{cases} \exp[-\Delta E/k_B T] & \text{if } \Delta E > 0 \\ 1 & \text{otherwise.} \end{cases} \quad (7)$$

As with MD simulation, the choice of interaction potential is central to the success of the MC method. However, for MC simulation, if the structure is of primary importance, there is a little more flexibility in how the potential may be constructed. Very simple nearest-neighbour interactions may be chosen to give a particular local conformation with computationally simple parametrization. Simple interactions permit larger configuration sizes. It is also possible to constrain the types of atom moves to moves along specific directions, moves that swap atoms etc. This has the effect of restricting the range of configurational space available to the simulation and may be justified in specific circumstances.

A typical algorithm for an MC simulation would consist of the following:

(1) Generate a starting configuration of N atoms of appropriate density and impose periodic boundary conditions. For crystalline materials, this will usually be a supercell of the crystal unit cell.
(2) Calculate the starting energy, E_{old}, based on the chosen potential functions.
(3) One atom is selected at random and moved a random amount and the energy is recalculated (E_{new}).
(4) If $\Delta E = E_{new} - E_{old}$ is below 0, then the move is accepted and the 'new' configuration becomes the 'old' configuration. If $\Delta E > 0$ then the move is accepted with probability $\exp[-\Delta E/k_B T]$.
(5) The process is repeated from step 3 until the energy does not, on average, reduce further and the simulation is said to have converged. The simulation is then repeated to collect statistically distinct configurations for averaging.

4.3. Reverse Monte Carlo modelling

In recent years the RMC modelling method has been used extensively to investigate the local order in superionic conductors. Indeed, the first use of RMC on a crystalline system was to determine the atomic origin of the observed pre-melting behaviour in ion-conducting AgBr [48]. It was first developed to investigate the structures of liquid and amorphous materials by comparing correlation functions from a three-dimensional distribution of atoms with those determined experimentally [49]. Since then the technique has been widely used to characterize structural disorder in a wide variety of systems, including crystalline and amorphous superionic conductors. It has recently been reviewed in detail [50].

The algorithm used is identical to the MC algorithm described in section 4.2, except that instead of minimizing the energy of the atom configuration on the basis of potential functions, the difference between the experimental and calculated correlation functions is minimized. Formally, the function minimized is (for example)

$$\chi^2_{RMC} = \sum_k \sum_{i=1}^{N} [i_{Calc}(Q_i)_k - i_{Expt}(Q_i)_k]^2/\sigma_k^2(Q_i)$$

$$+ \sum_l \sum_{i=1}^{N} [G_{Calc}(r_i)_l - G_{Expt}(r_i)_l]^2/\sigma_l^2(r_i) + \sum_{j=1}^{m} (f_j^{Req} - f_j^{RMC})^2/\sigma_j. \quad (8)$$

Here χ^2 is composed of comparisons between calculations from the model and the k total scattering structure factors, $i(Q)$, the l total radial distribution functions, $G(r)$, and the values of the m constraints, f. The values of σ may be determined directly from the experimental errors, or the σ can be used as weighting terms, to emphasize a particular correlation function. They may also be iteratively reduced during the minimizing procedure, which is akin to simulated annealing (where an MC simulation is run and the temperature is iteratively reduced to attempt to produce a structure with the lowest energy). The third term on the right-hand side of equation (8) allows the modeller to incorporate constraints. These may be simple, e.g. defining the number of neighbours of a particular ion about another, or may be more complex, defining specific local geometries. More recently, the Bragg intensities have been used to constrain the RMC model [51], by introducing a constraint of the form

$$\sum_{hkl} (s|F_{hkl}|^2_{Expt} - |F_{hkl}|^2_{Calc})^2 / \sigma^2_{hkl}, \tag{9}$$

either using extracted Bragg intensities, or by profile fitting the Bragg diffraction pattern. This results in extremely reliable structural models that accurately describe the local disorder within the average structure.

5. Superionic systems

5.1. Superionic conductors with the fluorite structure

The fluorite structure consists of a simple cubic array of anions with a cation filling every other anion cube centre. This results in a fcc structure with cations at 4a (000) sites and anions at 8c $(\frac{1}{4}\frac{1}{4}\frac{1}{4})$ sites in space group $Fm\bar{3}m$. Several fluorite structured materials display a specific heat anomaly at a high temperature, T_C, which is ~80% of the melting transition temperature. This corresponds to a large, but continuous, increase in ionic conductivity, resulting from an increase in mobile ionic defects. These are all characteristics of a type II superionic transition. In addition, aliovalent doping with 3^+ (or 4^+) cations can lead to an increase in anion concentration and a decrease in T_C, whilst maintaining the fluorite lattice. Furthermore, the high-temperature fluorite structure of zirconia may be stabilized to room temperature by doping with aliovalent cations and with a corresponding reduction of anion density. This composite family of materials has been extensively studied using diffuse scattering and computer modelling, largely because of the underlying simplicity of the structure, the availability of large single crystals and, at least initially, their being model systems for the high-temperature behaviour of the fission material, UO_2 (see, for example, [52] and [53]).

There is not space in this review to summarize all the investigations into the structural disorder within this family of superionic materials and indeed much of the work has been reviewed recently [19]. The group based at Harwell, UK, in the 1970s and 1980s made extensive use of single-crystal diffuse neutron scattering and 'aggregated defect cluster' models to understand the disorder associated with the mobile ions in undoped fluorites at high temperature (see, for example, the work on β-PbF_2, $SrCl_2$ and CaF_2 [22], a later review [54] and figure 2). This was followed by later similar work on the doped fluorite $Ca_{0.94}Y_{0.06}F_{2.06}$ [55] and the related cubic-stabilized zirconias, Y_2O_3-doped ZrO_2 [24] and CaO-doped ZrO_2 [56]. Different defect clusters were responsible for the diffuse scattering in these systems, reflecting the different chemical compositions. At room temperature, the excess anions in $Ca_{0.94}Y_{0.06}F_{2.06}$ are accommodated within a cube–octahedral defect (figure 5) [57], whereas vacancies in anion-deficient Y_2O_3-doped ZrO_2 are found in single-vacancy, di-vacancy or aggregated di-vacancy clusters, depending on the degree of doping [24]. A different defect is found in CaO-doped ZrO_2 [56]. These are largely static defects, although the smaller
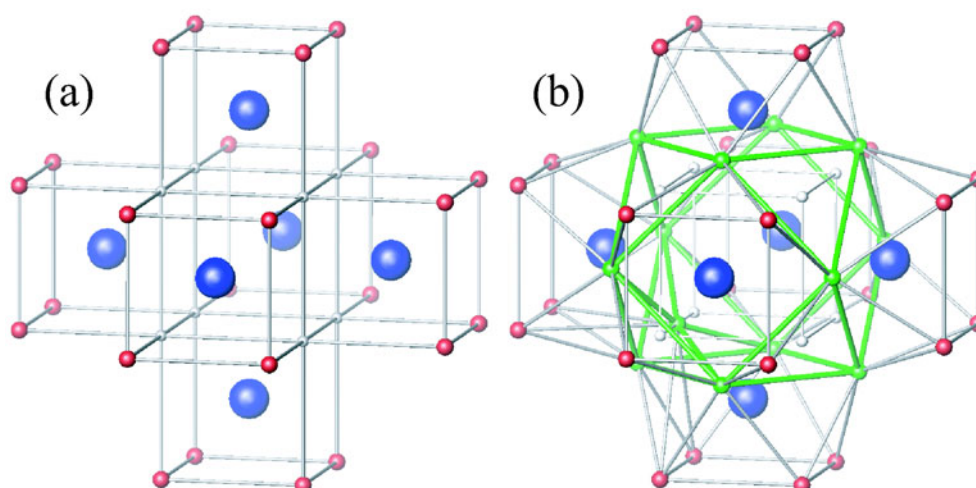
Figure 5. (a) A diagram showing part of the undistorted fluorite lattice consisting of six edge-sharing cation-filled anion cubes surrounding an empty cube. (b) The equivalent portion of the fluorite lattice distorted into six corner-sharing square anti-prisms. This arrangement incorporates at least four additional anions around the inner empty cavity and forms the so-called cube–octahedral defect cluster used to explain the diffuse scattering in $Ca_{0.94}Y_{0.06}F_{2.06}$ [55]. The positions of the original anions, now anion vacancies, are also shown in (b) for completeness. Cations and anions are shown as large and small spheres, respectively.

defects may become mobile at higher temperatures, like the small mobile defects found in the undoped systems at high temperature. The temperature and dopant concentration dependence of the diffuse scattering gives important information on the relative influences of different defect clusters on the superionic conductivity of doped and undoped fluorite superionic conductors.

X-ray diffuse scattering has also been used to complement the neutron diffuse scattering (e.g. [24] and [56]), although the relatively weak scattering of light anions in the presence of strong scattering from the heavier cations means that the x-ray signal is dominated by the cation sublattice. The weakly scattering anions have been used to an advantage in an x-ray diffuse scattering study of Y_2O_3-doped ZrO_2 [58]. To a first approximation, as far as x-ray scattering is concerned, Y_2O_3-doped ZrO_2 appears like a binary alloy composed of Y and Zr. Additionally, the similarity of Zr and Y x-ray scattering factors means that only the term associated with the mean squared atomic displacements contributes significantly in the general expression for diffuse scattering from a disordered alloy [59]. As a result, the x-ray diffuse scattering could be interpreted in terms of the lattice expanding away from Y cations and contracting towards Zr cations. This interpretation would be very difficult using neutron diffuse scattering, where, although Zr and Y also possess very similar neutron scattering lengths, the scattering signal is enhanced by additional correlations involving the anions and the simple theories based on diffuse scattering from binary alloys would be inappropriate.

Welberry and co-workers have extended their earlier work to utilize a number of interpretative methods, some of which are summarized in [60]. One of their approaches was to use a two-stage sequential MC algorithm to generate a three-dimensional model of $Zr_{0.61}Y_{0.39}O_{1.805}$ [61]. To construct their model, the oxygen vacancies were first ordered on a $64 \times 64 \times 64$ array ($32 \times 32 \times 32$ unit cells) using near-neighbour pair interactions designed to mimic expected local vacancy atom structures. The second stage of the MC simulation involved relaxing the cation positions using a harmonic potential, $E = k(d - d_0)^2$, where d is
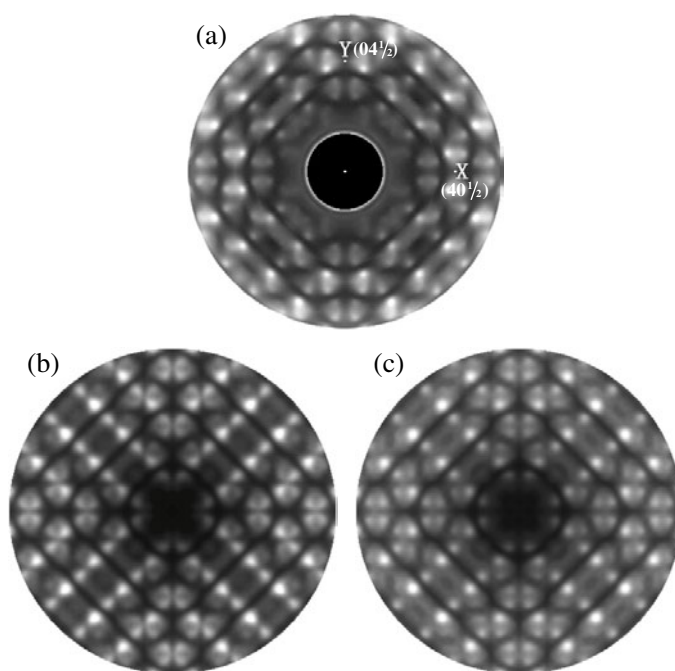
Figure 6. (a) X-ray diffuse scattering in the $(hk\frac{1}{2})$ reciprocal-lattice plane of yttria-stabilized cubic zirconia. X and Y mark the points $(40\frac{1}{2})$ and $(04\frac{1}{2})$, respectively. (b) The equivalent reciprocal-lattice plane calculated from a two-stage MC simulation as described in the text. By way of comparison, (c) is determined from a model where the vacancy distribution is determined directly using a modulation wave synthesis. The distortions around the vacancies are then introduced into the model in the same way as in (b). After [60–62].

the distance between two neighbouring cations and d_0 depends on whether the two cations are interspersed by an oxygen atom or vacancy. Following this, the diffuse x-ray scattering was calculated using only the cation positions (see above) and compared with the measured data (see figure 6). The arrangement which gave the best agreement with the diffuse scattering data was one where the vacancies are ordered to avoid nearest-neighbour $(1/2)\langle 100 \rangle$ pairs, next-nearest-neighbour $(1/2)\langle 110 \rangle$ pairs and third-nearest-neighbour $(1/2)\langle 111 \rangle$ pairs across empty cube centres, but to allow $(1/2)\langle 111 \rangle$ pairs across cation-filled cube centres. This vacancy–vacancy arrangement is consistent with a number of ordered fluorite-related superstructures.

In a related work, a modulated wave approach was used to generate the structural model, resulting in a similar ordering scheme [62] (see figure 6(c)). Most recently, there have been investigations of how effective RMC modelling may be when applied to cubic-stabilized zirconia using single-crystal diffuse x-ray scattering (see for example [63] and [64]). This work is more of a critique of the RMC method, as applied to single-crystal diffuse scattering, rather than giving additional insight into the defect structure of cubic-stabilized zirconia. Hence it will not be discussed further here. Finally, the local environment about specific ions can be probed effectively with EXAFS, and this technique has been used to investigate the bond lengths and coordinations around the cations in a whole series of cubic-stabilized zirconias with complex dopants [65].
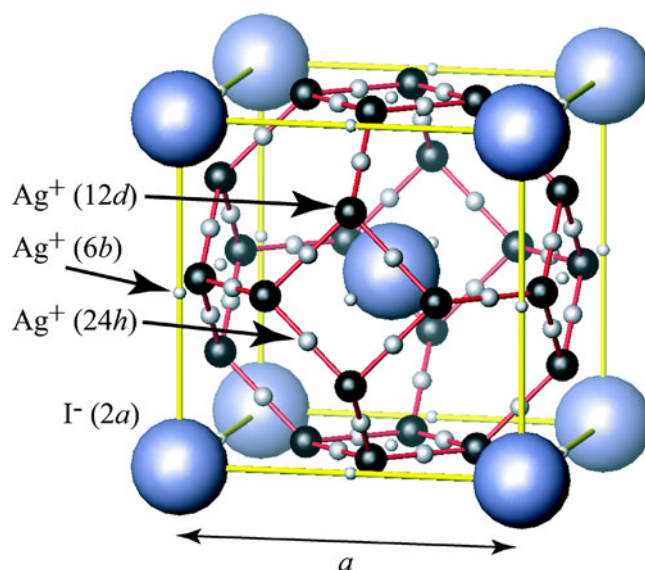
Figure 7. A plot showing the unit cell of α-AgI. The site labels are defined in bcc space group $Im\bar{3}m$. The most probable cation lattice sites are shown as larger, darker spheres.

5.2. Crystalline copper and silver-based superionic conductors

The crystalline copper and silver halide and chalcogenide superionic conductors are another large class of much-studied superionic conductors. They are predominantly based on two structure types consisting of a body-centred cubic (bcc) or fcc anion sublattice and disordered cations. The former results in the α-AgI structure and the latter are disordered structures based on the zinc-blende or rock-salt structure types.

5.2.1. Systems with the α-AgI bcc structure.

There have been many studies of the disorder in α-AgI, spanning most of the last century, and encompassing virtually every experimental and theoretical approach (see [66] or [19]). Experimental investigations include neutron total scattering [67], x-ray diffuse scattering [68] (both on powdered samples), single-crystal diffuse scattering (e.g. x-ray [69] and neutron [70]) and EXAFS [39, 71]. Models have been calculated using MD simulations, based on a two-body RVP effective interatomic potential (section 4.1.1, [45]), MC simulations (e.g. [72]) and RMC modelling [67]. The key structural issue is understanding how the silver ions are accommodated within the bcc iodine sublattice. This may then be used to deduce the cation migration pathways within the lattice, which give rise to the exceptionally high ionic conductivity. The α-AgI structure is shown in figure 7. The two silver ions per unit cell are distributed between 42 possible lattice sites, although the general consensus is that the sites are occupied in the preference order 12d(tetrahedral) > 24h(trigonal) > 6b(octahedral) in space group $Im\bar{3}m$. Hence conduction takes place between tetrahedral sites via trigonal sites, with only a small occupation of octahedral sites.

Recent high-pressure studies have shown that CuCl and CuI also possess a phase with the α-AgI structure at high temperature and high pressure [73, 74]. This is in addition to CuBr, which has an α-AgI structured phase just below melting at ambient pressure [75]. It is slightly surprising that this phase may be stabilized by high pressure and high temperature,

when superionic materials are generally thought to have low-density structures. However, the α-AgI structure is actually more dense than the lower temperature fcc (or hcp) structures found in these copper and silver binary halides. This emphasizes the suitability of the α-AgI structure for superionic conduction; even though it is denser than the equivalent superionic fcc structures, the conductivity is still higher.

5.2.2. System with the α-CuI fcc structure. Similarly comprehensive work has been carried out on α-CuI, including neutron total scattering measurements [76], EXAFS measurements [39], RMC modelling [76] and MD simulations [77]. α-CuI consists of a fcc anion sublattice with the four cations per unit cell principally distributed between the eight available tetrahedral interstices, in space group $Fm\bar{3}m$ [78]. Two controversies may be highlighted with reference to this superionic phase. The first concerns the details of the ionic conduction mechanism in fcc systems. Tetrahedral cavities within the fcc structure share common faces with neighbouring octahedral cavities whereas neighbouring fcc cavities are linked by cavity edges. As a result, the cation conduction mechanism has been thought to follow a tetrahedral site $\leftrightarrow$ octahedral site $\leftrightarrow$ tetrahedral site etc pathway. This mechanism was confirmed by a polyhedral analysis (whereby a cation is assigned to a particular site if it resides within the polyhedron defined by anions that are nearest neighbours to that site) of EXAFS measurements that suggested that $\sim$30% of the cations reside in octahedral sites [39]. However, a distinction should be drawn between a cation residing *in* an octahedral *cavity* and residing *on* an octahedral *site* in the centre of the cavity. This is because more recent Rietveld refinements of the average structure find no evidence for occupation of octahedral sites, but instead large anharmonic displacements about tetrahedral sites, which are largest in the $\langle 111 \rangle$ directions towards the octahedral sites [78]. The distribution of cations is such that, on average, some cations will be in octahedral cavities, but not necessarily on the octahedral site. This distinction is clearly explained with reference to a MD simulation, which found $\sim$35% cations in octahedral cavities but only a few per cent on the octahedral site [79], although they subsequently used a polyhedral analysis to 'confirm' the tetrahedral site $\leftrightarrow$ octahedral site $\leftrightarrow$ tetrahedral site conduction pathway. This interpretation was then challenged by another MD study [77]. This study obtained similar ion distributions but, by tracking individual cations, showed that the ions actually diffuse directly from tetrahedral to tetrahedral site in a $\sim \langle 100 \rangle$ direction through the edge of the octahedral cavity and not via an octahedral site at all.

The above discussion may be concerned with a subtle distinction in the definition of the location of the diffusing cations, but it has important implications on how the conduction mechanism may be understood. If the tetrahedral site $\leftrightarrow$ octahedral site $\leftrightarrow$ tetrahedral site pathway is accepted, then it must be assumed that the cation can be assigned a genuine octahedral coordination. This is not very favourable for copper halides and indeed high pressures are required to transform the copper halides into an octahedral arrangement [80, 81]. If the mechanism is via the edges of the octahedral cavity, the cations diffuse via distorted 'tetrahedral' coordinations with three anions. The diffusion is never directly across the centre of the octahedral cavity and the preferred tetrahedral arrangements are preserved.

The second controversy concerns the ability of the RVP potential to reproduce the local structural environment reliably. Differences have been observed in the low-r features of the partial pair correlation function, $g_{Cu-Cu}(r)$, of superionic α-CuI, obtained from RMC modelling of total scattering data and MD simulations using an RVP potential [76]. As can be seen in figure 8, a peak is observed at low r in the RMC results, which is not found in the MD results. It is suggested that this difference arises because the MD simulation cannot reproduce the low-r peak in $g_{Cu-Cu}(r)$ without distorting the CuI environment. Such polarization effects may only be reproduced using additional three-body terms in the potential used for the MD simulations.
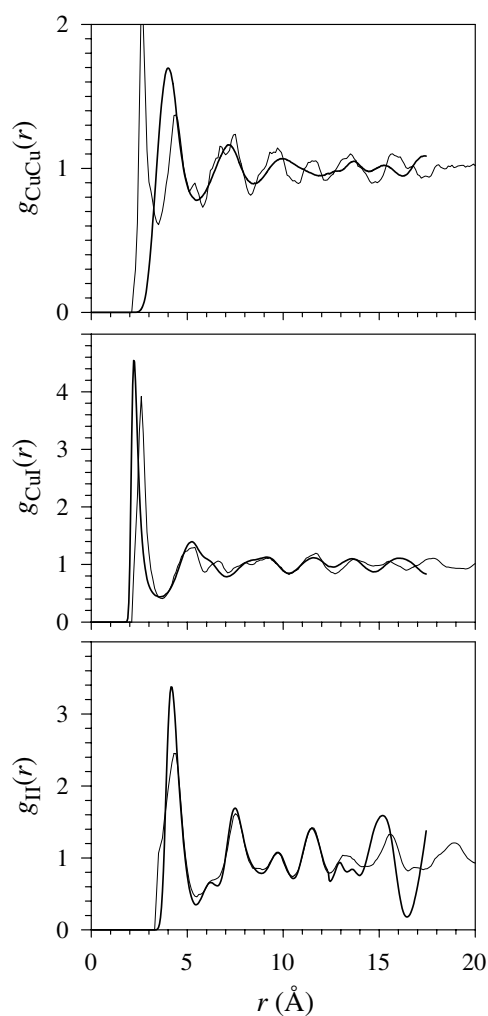
Figure 8. Partial radial distribution functions of α-CuI determined from MD simulations (thick curves) and RMC modelling (thin curves) (after [77] and [76] respectively).

This demonstrates that although the RVP potential does reproduce many of the characteristics of the superionic process in these materials, it is nonetheless only an effective two-body parametrization of the true inter-ionic potentials. Further evidence of this difference has been observed when comparing MD results with partial radial distribution functions obtained from RMC modelling and isotopic substitution experiments on the silver chalcogenide superionic systems (see section 5.2.4) [82–84].

5.2.3. Systems with the AgBr rock-salt structure.   Before moving on to more complex copper- and silver-based superionic conductors, a brief mention should be made of the silver halides with the rock-salt structure. AgBr and AgCl both display more ionic character than the other copper and silver halide superionic materials and both possess the rock-salt structure at room temperature and pressure. Here the cations reside in the octahedral sites of the anion fcc lattice. The ionic conductivity increases anomalously as the materials approach their
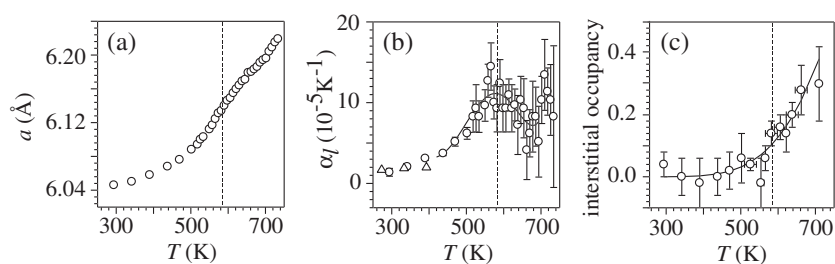
Figure 9. The temperature dependence of (a) the cell parameter, (b) the linear expansivity and (c) the cation occupation of tetrahedral interstitial sites of rock-salt structured AgI at 1.1 GPa (from [91]).

respective melting points, achieving high values, but without a clear superionic transition. The increase in conductivity is associated with an increased cation occupation of tetrahedral interstices [85] and a collinear interstitialcy mechanism is responsible for the ionic conduction, whereby a tetrahedral interstitial cation displaces a neighbouring cation from an octahedral site into another tetrahedral interstice in a linear ⟨111⟩ direction [86]. However, the number of tetrahedral interstitial cations remains small and unsaturated, even just below melting (∼4% cation interstitials are found in AgBr 1 K below T_M [87]), and the behaviour has been ascribed to a 'pre-melting' effect [88]. The nature of the short-range correlations has been the subject of recent discussion with regard to high-quality EXAFS results from both the Ag and Br K edges (see [89] and references therein). Using modern interpretative methods, this work questions the accuracy of the near-neighbour correlations obtained by RMC modelling [87] and MD simulations [90] (and incidentally again highlights the low-r differences in the MD- and RMC-generated partial radial distribution functions of the conducting ion—in this case, $g_{Ag-Ag}(r)$). This shows that descriptions of the local structure associated with ionic conduction, even for disordered materials with simple rock-salt structures and small number of defects, are hard to characterize robustly.

AgI also has a rock-salt structured phase at pressures above ∼0.4 GPa [91]. The ionic conductivity of this phase also increases anomalously with increasing temperature, although it does begin to saturate just before transforming into the α-AgI phase [92]. Diffraction measurements show that this superionic region of the rock-salt phase corresponds to ∼30% cation occupation of tetrahedral sites (see figure 9). The high ionic conduction, together with a saturation of interstitial defects and an anomalous lattice expansion, confirm that rock-salt structured AgI has a type II superionic transition [91]. This is the only silver or copper halide material which displays a clear type II superionic transition and as such it has similarities with the undoped fluorite superionic materials such as β-PbF$_2$. Some have argued that a superionic transition would occur in AgBr and AgCl at high temperatures; only melting of the anion sublattice interrupts it [93]. Others have been able to characterize the order of the superionic (and melting) transitions on the basis of the defect–defect interactions in the different materials [94].

5.2.4. The silver chalcogenide superionic conductors. The silver chalcogenides (Ag$_2$S, Ag$_2$Se and Ag$_2$Te) also have superionic phases which are similar to the silver and copper binary halides except that there are twice as many cations to fill the available voids in the anion sublattices. All three compounds have α-AgI-like bcc superionic phases and Ag$_2$S and Ag$_2$Te also have fcc superionic phases [19]. Unusually, and even though the bcc phase of

Ag_2Te occurs at higher temperatures than its fcc phase (in common with the case for the copper and silver halides), the bcc phase of Ag_2S occurs at *lower* temperatures than its fcc phase [95]. To date, this difference has not been explained adequately. The increased number of cations per anion means that local cation ordering is more likely and octahedral sites are more likely to be occupied in addition to the tetrahedral sites. This local ordering results in structured diffuse scattering, measured for β-Ag_2S using x-ray diffraction [96] and elastic neutron scattering [97]. Diffuse disc-like features are observed at $q \sim (0.6, 0, 0)$ away from Bragg positions with a strong peak at $Q = (1.6, 1, 0)$. The widths of this feature in reciprocal space were used to construct a static model of the cation local ordering on distinct tetrahedral sites [96]. This was later countered by the neutron measurements, which demonstrated that the diffuse scattering was almost entirely quasielastic in origin and hence must originate from dynamic, rather than static, correlations [97]. These measurements were supported by a number of MD simulations using RVP potentials during the 1980s, the most comprehensive of which was on Ag_2Se [82]. The simulation results were compared with the diffuse scattering experiments on Ag_2S reflecting the close similarity between these phases. More recently there has been an *ab initio* MD simulation study of Ag_2Se, largely concentrating on the liquid state [98].

The recent experimental work on the silver chalcogenides has concentrated on powdered samples, including total scattering measurements on Ag_2Te, analysed using RMC [83] and total scattering with neutron isotopic substitution on Ag_2Se [84] (see also related work on liquid Ag_2Se [99] and Ag_2Te [36]). The former measured total scattering structure factors, $i(Q)$ (equation (3)), for each of the three phases of Ag_2Te at or above room temperature. There were some inconsistencies in the details of the average structures obtained from the Rietveld refinements and RMC models, probably due to the basic implementation of the RMC method used (the Bragg intensities were not considered) and the restrictive nature of the Rietveld-refined average split-site model. Of particular note is the nature of the cation occupation of the octahedral sites in the fcc α-phase (space group $Fm\bar{3}m$). Both techniques find evidence of significant occupation of the octahedral cavity, in contrast to the less cation-dense α-CuI phase. However, Rietveld results suggest that the cations reside off-centre from the $(\frac{1}{2}\frac{1}{2}\frac{1}{2})$ octahedral site and instead are distributed between (xxx) positions, with $x \sim 0.4$. The RMC models do not make this distinction, and the average density peaks at the site centre (i.e. $(\frac{1}{2}\frac{1}{2}\frac{1}{2})$).

The ion distribution within the tetrahedral and octahedral sites has also been investigated for the isostructural fcc phase of α-Ag_2S [95]. This is the highest-temperature phase of Ag_2S and the powder neutron diffraction data measured at 929 K only show six clear Bragg peaks. Rietveld refinement of the data show occupation of both tetrahedral and octahedral sites, but the data are not good enough to distinguish clearly between models with cations located at $(\frac{1}{2}\frac{1}{2}\frac{1}{2})$ ($\chi^2 = 1.10$) or distributed over (xxx) positions, with $x \sim 0.4$ ($\chi^2 = 1.08$). However, MaxEnt Fourier reconstructions of the ion density show that the distribution, although peaking at $(\frac{1}{2}\frac{1}{2}\frac{1}{2})$, is anisotropic and spreads significantly in $\langle 111 \rangle$ directions (figure 10(a)). MD simulations, using RVP potentials determined previously [100], support this cation distribution (figure 10(b)).

There is better consensus concerning the nature of the disorder in the highest-temperature bcc γ-phase of Ag_2Te, which is found to be analogous to α-AgI. Both Reitveld and RMC average models place most cation density in the tetragonal sites and conduction takes place between tetrahedral sites via trigonal sites in $\langle 110 \rangle$-type directions, with little occupation of the octahedral sites. This is contrasted with what is found in bcc β-Ag_2S and α-Ag_2Se, where octahedral occupation is found, albeit at much lower temperatures and with the observation that the octahedral occupation decreases with increased temperature. MaxEnt Fourier reconstructions of the ionic density in β-Ag_2S show the cation density at the $(\frac{1}{2}\frac{1}{4}0)$
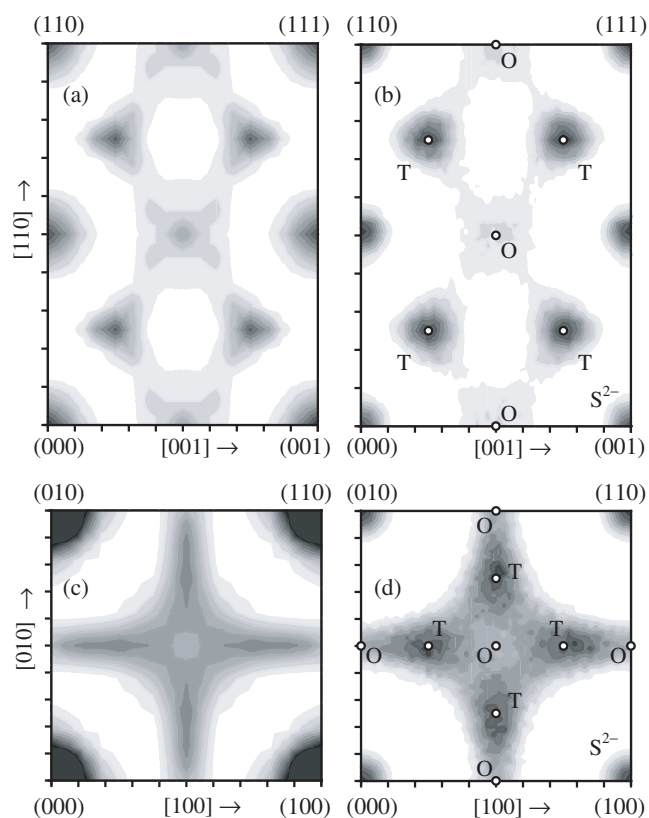
Figure 10. Average density distributions within the fcc α-Ag$_2$S (upper plots) and bcc β-Ag$_2$S unit cells (lower plots). MaxEnt Fourier reconstructions and results from MD simulations are shown on the left- and right-hand sides, respectively. Temperatures are (a) 929(2) K, (b) 900 K, (c) 558(2) K and (d) 550 K (from [95]).

tetrahedral sites elongated in $\langle 100 \rangle$ directions towards neighbouring $(\frac{1}{2}\frac{1}{2}0)$ octahedral sites, but the octahedral site cation density is lower than that of nearby trigonal $(xx0)$ positions (figure 10(c)). However, with $x \sim 0.45$, this is very close to the octahedral site [95]. These results have also been compared with the density distribution obtained from MD simulations of β-Ag$_2$S (figure 10(d)).

The RMC-generated partial radial distribution functions, $g_{ij}(r)$, for bcc γ-Ag$_2$Te at 1073 K may be compared with those obtained for bcc α-Ag$_2$Se at 1073 K using neutron isotopic substitution measurements [84] and at 435 K using MD simulations [82]. In a neutron isotopic substitution measurement, total scattering measurements are made on samples with the same chemical composition, but different isotopic composition. Provided that isotopic enrichment of the sample is practically possible and that there is enough contrast between the neutron scattering lengths of the different isotopes, the data may be used to separate the contributions from the different pair correlations experimentally. The resulting partial radial distribution functions, $g_{ij}(r)$, are independent of any modelling or simulation. In this measurement [99], three different isotopically labelled samples were used, ^{107}Ag$_2$^{76}Se, ^{109}Ag$_2$^{N}Se and ^{N}Ag$_2$^{76}Se, where ^{N} refers to the element with natural isotopic abundance. The corrected total scattering structure factors, $i(Q)$, are composed of weighted sums of the Faber–Ziman partial structure

factors, $A_{ij}(Q)$ [35], the weighting being dependent on the isotopic composition and relative abundance of the components. In this particular case,

$$
\begin{aligned}
{}^{107}_{N}i(Q) &= 0.2594(19)[A_{\mathrm{AgAg}}(Q) - 1] + 0.2706(14)[A_{\mathrm{AgSe}}(Q) - 1] \\
&\quad + 0.0706(1)[A_{\mathrm{SeSe}}(Q) - 1] \\
{}^{109}_{76}i(Q) &= 0.0780(8)[A_{\mathrm{AgAg}}(Q) - 1] + 0.2272(25)[A_{\mathrm{AgSe}}(Q) - 1] \\
&\quad + 0.1654(19)[A_{\mathrm{SeSe}}(Q) - 1] \\
{}^{N}_{76}i(Q) &= 0.1559(3)[A_{\mathrm{AgAg}}(Q) - 1] + 0.3211(27)[A_{\mathrm{AgSe}}(Q) - 1] \\
&\quad + 0.1654(19)[A_{\mathrm{SeSe}}(Q) - 1]
\end{aligned}
\tag{10}
$$

where ${}^{X}_{Y}i(Q)$ refers to the total scattering structure factor of ${}^{X}\mathrm{Ag}_2{}^{Y}\mathrm{Se}$. Matrix inversion of the above equations gives $A_{ij}(Q)$ in terms of the ${}^{X}_{Y}i(Q)$ and Fourier transformation of the $A_{ij}(Q)$ gives the partial radial distribution functions, $g_{ij}(r)$.

The different $g_{ij}(r)$ are shown in figure 11. There is clearly good agreement between the RMC-generated results for γ-Ag$_2$Te and the isotopic substitution results for α-Ag$_2$Se, and reasonable agreement with the MD results for α-Ag$_2$Se, although again there is some discrepancy in the lowest-r peak in $g_{\mathrm{AgAg}}(r)$. It has also been observed that there is a strong similarity between the $g_{ij}(r)$ (or $A_{ij}(Q)$) for the high-temperature superionic crystalline phase and for the liquid just above the melting point, particularly for $g_{\mathrm{AgAg}}(r)$ [36]. This suggests that common local structural arrangements exist in the disordered solid and liquid phases and further emphasizes the 'liquid-like' nature of the disorder associated with superionic conduction in these systems.

5.2.5. Other doped copper and silver superionic conductors.

Since chemical doping has been found to improve the superionic properties at lower temperatures, there have been many investigations of doped materials based on the AgI or CuI parent compounds. The structures of the most promising have also been investigated in detail. Here we shall only discuss three basic systems, Ag$_3$SI, A$_4$MI$_5$ (A = Ag or Cu, M = Rb or K) and Ag$_2$MI$_4$ (M = Hg or Pb). This is by no means an exhaustive list, but will serve to illustrate some of the structural issues associated with chemical doping.

### 5.2.5a. Silver sulphur iodide, Ag$_3$SI.

Ag$_3$SI, with $1\frac{1}{2}$ cations per anion, has a cation density midway between the silver halide and silver chalcogenide superionic conductors. It possess three distinct phases. The low-temperature rhombohedral γ-phase transforms at $T = 157$ K to the primitive cubic β-phase. This phase in turn transforms to the bcc α-phase at $T = 519$ K. Furthermore, the high-temperature α-phase may be quenched to room temperature and below by fast cooling, to a phase denoted α^*-Ag$_3$SI. The conductivity changes by many orders of magnitude within the γ-phase, with values of $\sigma \sim 10^{-8}$ Ω^{-1} cm^{-1} at 100 K and $\sigma \sim 10^{-5}$ Ω^{-1} cm^{-1} just below the γ–β phase transition, $T_{\gamma-\beta}$ [101]. There is a small fourfold increase in σ at $T_{\gamma-\beta}$, above which the increase with temperature is more gradual, achieving a value of $\sigma \sim 10^{-2}$ Ω^{-1} cm^{-1} at room temperature. This compares with a value of $\sigma \sim 0.3$ Ω^{-1} cm^{-1} for α^*-Ag$_3$SI at room temperature [102]. The conductivity only increases slowly within the α-phase. The conductivity of Ag$_3$SI therefore changes by more than eight orders of magnitude between 100 and 519 K and possesses two phases at room temperature, one stable and one metastable, with good and very good ionic conductivity, respectively.

The significant structural disordering mechanisms associated with such a large change in conductivity have been investigated using Rietveld and total scattering methods [101, 103]. The structures are summarized in figure 12. In the α-Ag$_3$SI phase the anions are fully disordered
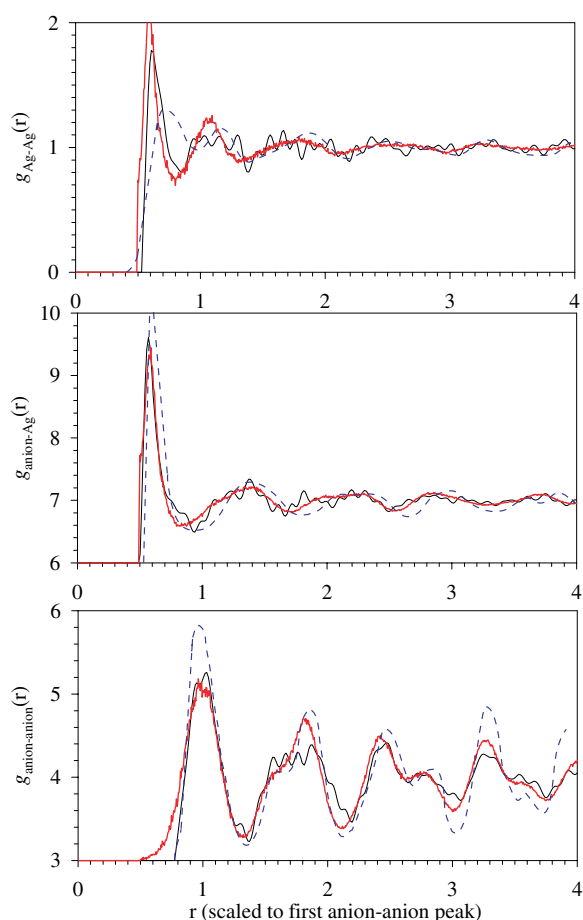
Figure 11. A comparison of the partial radial distribution functions for various bcc silver chalcogenides. Thin, full, smooth curves correspond to α-Ag_2Se at $T = 1073$ K (neutron isotopic substitution [84]); thick, full curves to γ-Ag_2Te at $T = 1073$ K (RMC refinement of neutron total scattering data [83]); dashed curves to α-Ag_2Se at $T = 435$K (MD simulation [82]). Each data set has been scaled to the first peak in the $g_{anion-anion}(r)$ to account for density differences.

between 2(a) sites at (000) and $(\frac{1}{2}\frac{1}{2}\frac{1}{2})$ on the bcc $Im\bar{3}m$ lattice. This disorder is retained on quenching to α^*-Ag_3SI, although the diffuse scattering suggests that some short-range anion ordering takes place, presumably dependent on cooling rates. In contrast, the β-phase has a fully ordered anion lattice, with S^{2-} in 1(a) sites at (000) and I^- in 1(b) sites at $(\frac{1}{2}\frac{1}{2}\frac{1}{2})$ in the primitive cubic space group $Pm\bar{3}m$. This ordered anion sublattice then distorts to form the rhombohedral structure of γ-Ag_3SI with the S^{2-} ion moving from (000) along the body diagonal to (xxx) with $x \sim 0.04$. The key to understanding the ionic conductivity rests on the way that the cations populate these distinct anion sublattices. In the α-phase, the cation density is distributed between the 24(h) $(xx0)$ sites with $x \sim 3/8$. The atomic displacement parameters are highly anisotropic such that the distribution appears as a disc centred on each octahedral site of the structure (although not peaking at the site) and elongated in the directions perpendicular to the short cation–anion contact. The anion ordering in the β-phase results in the cations occupying half the number of sites, i.e. 12(h) $(\frac{1}{2}y0)$ sites with $y \sim 0.9$. Again
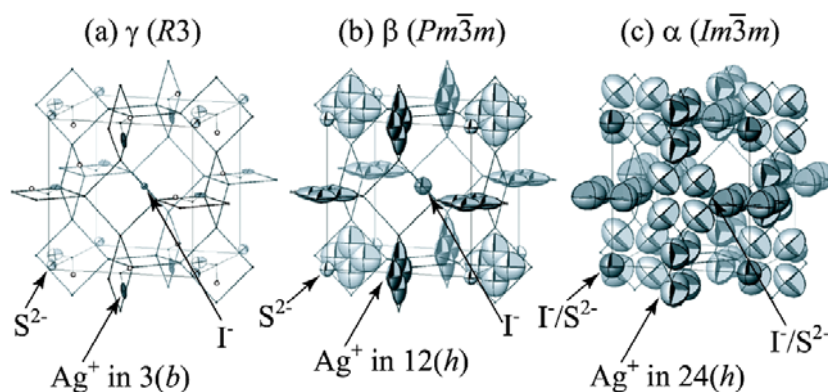
Figure 12. Schematic representations of the crystal structures of three phases of Ag_3SI (after [101]). Each plot shows the unit cell and the network of tetrahedral sites within the structure. (a) γ-Ag_3SI at $T = 10(1)$ K (the alternative Ag2 sites which become $\sim$10% occupied just below the γ–β transition are shown as open circles); (b) β-Ag_3SI at $T = 297(2)$ K; (c) α-Ag_3SI at $T = 569(2)$ K.

this is accompanied by anisotropic atom displacement parameters to give a similar apparent distribution to that of α-Ag_3SI, but only occupying locations around the octahedral sites with short S^{2-}–Ag^+ and long I^-–Ag^+ contacts. In both these phases all the cations are mobile, resulting in high values of ionic conductivity. The conductivity is higher in the α-phase than the β-phase because there are more sites available per cation and the sites are closer together.

The β–γ transition is a little more subtle. Specific heat measurements show that this transition has a λ-type anomaly, indicative of a second-order phase transition [104]. This is inconsistent with the discontinuous changes in the lattice expansion and ionic conductivity [101]. Diffraction measurements [103] show that on cooling through $T_{\gamma-\beta}$ the cations order onto two sets of 3(b) (xyz) sites in space group $R3$. The majority are on site Ag1 ($\sim$0.5, $\sim$0.9, $\sim$0) with around 10% on Ag2 ($\sim$0.5, $\sim$0, $\sim$0.9). Further cooling increases the distortion of the anion lattice and fully orders the cations onto the Ag1 site at low temperature. The phase transition therefore occurs when the cations preferentially occupy six of the twelve possible cation sites in the β-phase, thus destabilizing the anion lattice; further cooling then gradually orders the cations onto three of the six cation sites that were initially occupied just below $T_{\gamma-\beta}$. The conductivity within this phase increases rapidly with increasing temperature from a low value as a result of the increase of available conducting cations within the lattice. In summary, the cations begin fully ordered in the γ-phase at low temperature (one site/cation). On heating, this increases to two sites/cation (γ-phase, high temperature) to four sites/cation (β-phase) and finally to eight sites/cation (α-phase). The ionic conductivity increases accordingly.

5.2.5b. Silver rubidium iodide, RbAg₄I₅, and related materials. Isovalent substitution of Rb^+ for Ag^+ in AgI produces $RbAg_4I_5$, which is a superionic conductor at room temperature, with $\sigma = 0.21$ Ω^{-1} cm^{-1}. It is also isostructural with KAg_4I_5 and KCu_4I_5 [10]. KAg_4I_5 is stable above $T \sim 311$ K and metastable for a time at room temperature in a dry atmosphere, with a room temperature conductivity of $\sigma = 0.08$ Ω^{-1} cm^{-1}. KCu_4I_5 is stable above $T \sim 530$ K. Recent powder neutron diffraction [10] shows that all three are cubic ($a \sim 11$ Å), with the anions adopting the β-Mn structure. Their structures may be described in space group $P4_132$ (or its enantiomorph $P4_332$). The distorted octahedral cavities within the anion lattice are occupied by the non-diffusing monovalent dopant cation (Rb^+ or K^+) and the Ag^+ ions are
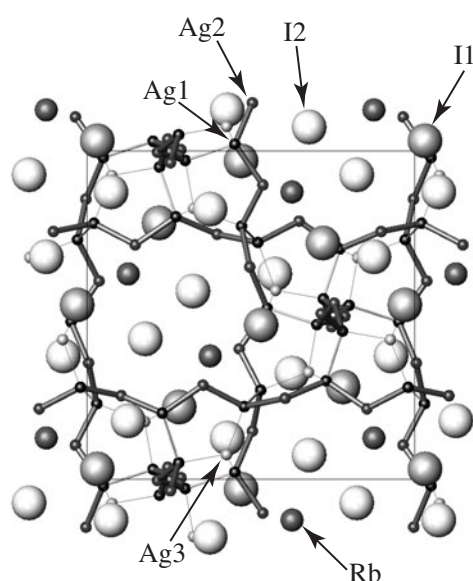
**Figure 13.** A projection down (001) of the average structure of RbAg$_4$I$_5$. Of the five proposed sites for Ag$^+$, Ag1 (black), Ag2 (grey) are significantly occupied, with a small occupancy of Ag3 (white). Bold lines indicate the infinite non-intersecting chains of $\cdots$ Ag1–Ag2–Ag1 $\cdots$ sites parallel to each of the cubic axes; medium lines show the likely route for conductivity between the linear channels; thin lines correspond to an alternative interchannel route via Ag3 sites (from [10]).

distributed between the three distorted tetrahedral cavities, although they preferentially occupy the tetrahedral sites labelled Ag1 and Ag2 over those labelled Ag3 in figure 13. The structure therefore contains one-dimensional channels of linked Ag1 and Ag2 tetrahedral cavities along the three $\langle 100 \rangle$ directions (see figure 13).

In order to help assess the likely conduction pathways within this structure, the MaxEnt Fourier difference method has been used to determine the most probable location of the Ag$^+$ ions with respect to the known I$^-$ and Rb$^+$ (or K$^+$) positions. A section $(0.45 \leqslant z \leqslant 0.55)$ of the MaxEnt reconstruction of the structure is shown in figure 14. This clearly shows Ag$^+$ ion density linking Ag1 and Ag2 sites in the one-dimensional channel running along the [100] direction at $y \sim 0.75$. In addition, there is significant density joining this channel with the two Ag1 sites at (0.22, 0.95, 0.48) and (0.72, 0.55, 0.52). These sites are parts of two channels running perpendicular to the section shown in figure 14, indicating that a network of *linked* one-dimensional channels form the conductivity path in RbAg$_4$I$_5$, KAg$_4$I$_5$ and KCu$_4$I$_5$. The conducting channels have also been investigated using bond valence summation mismatches [17]. There is strong similarity in the form of the conduction channels generated by the MaxEnt Fourier difference and bond valence summation methods. However, the former emphasizes the channels directly linking the sites that are occupied on average, and the latter highlights the unoccupied sites that also have low bond valence mismatch as possible conduction routes.

5.2.5c. Ag$_2$HgI$_4$ and related materials. Finally in this section, the effects of doping AgI and CuI with aliovalent Hg^{2+} and Pb^{2+} to produce the compounds Ag$_2$HgI$_4$, Cu$_2$HgI$_4$, Ag$_2$PbI$_4$ and Ag$_4$PbI$_6$ are compared. For this discussion the descriptions given in recent neutron diffraction
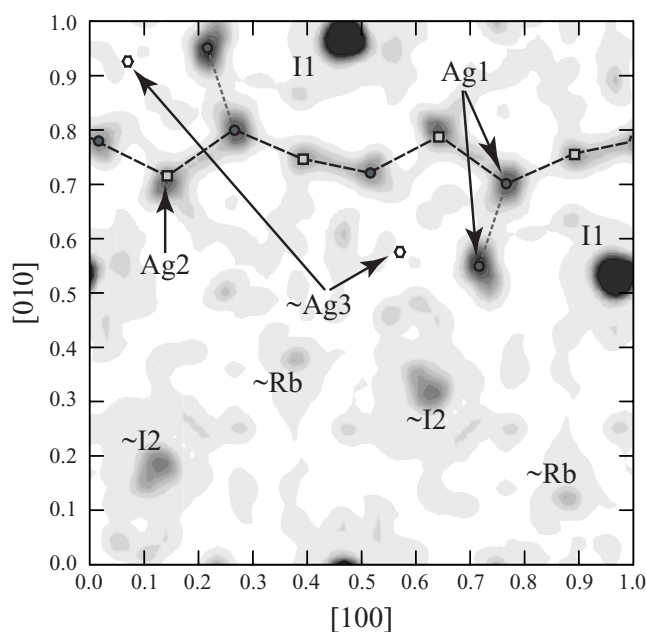
Figure 14. A (001) section through the maximum entropy Fourier reconstruction of the average density in $RbAg_4I_5$, with $0.45 \leqslant z \leqslant 0.55$. The conduction channel along one of the $\cdots$ Ag1(circles)–Ag2(squares)–Ag1 $\cdots$ chains is shown by the dotted curve at $y \sim 3/4$. The density between the Ag1 sites (at, for example, 0.72, 0.55, 0.52 and 0.77, 0.70, 0.47) indicates that Ag^+ may hop between the channels via this route. The Ag3 sites (hexagons) do not appear to contribute to any conduction pathway (see [10] for details). Sites labelled $\sim$I2, $\sim$Rb and $\sim$Ag3 are just outside this (001) section.

work [105–107] are followed. The two Hg^{2+}-doped compounds transform at 326 K (Ag_2HgI_4) or 338 K (Cu_2HgI_4) from their different tetragonal low-temperature structures to superionic α-phases, both with cation-deficient zinc-blende structures. The cations in the α-phases are distributed over the 4(c) sites at $(\frac{1}{4}\frac{1}{4}\frac{1}{4})$ with the anions in 4(a) sites at (000) in space group $F\bar{4}3m$. The cations do not appear to disorder significantly onto the other 4(d) tetrahedral sites at $(\frac{3}{4}\frac{3}{4}\frac{3}{4})$ or the octahedral sites at 4(b) $(\frac{1}{2}\frac{1}{2}\frac{1}{2})$. Hence the conduction is reasonably high merely because of the excess number of 4(c) sites per cation. At still higher temperatures, a wurtzite structured δ-phase is stabilized (above $\sim$410 and $\sim$578 K for Ag_2HgI_4 and Cu_2HgI_4, respectively). This structure is also disordered, but in contrast with the similar β-CuI structure, the anion sublattice is largely undistorted and the cation disorder suggests that ionic conduction takes place via octahedral voids. At temperatures above $\sim$445 K, a bcc ε-phase of Ag_2HgI_4 is formed with the α-AgI structure and little occupation of octahedral sites. A phase with this structure is not found at ambient pressure in Cu_2HgI_4.

AgI and PbI_2 combine at high temperatures to form a stable superionic phase for mixtures of composition $(AgI)_x$–$(PbI_2)_{1-x}$ with $2/3 > x > 4/5$. The structure of Ag_4PbI_6 ($x = 4/5$) and Ag_2PbI_4 ($x = 2/3$) is fcc in space group $Fm\bar{3}m$, above $\sim$400 and $\sim$420 K, respectively. In both compounds, the cations (Ag^+, Pb^{2+} plus vacancies, in different proportions) are principally on 4(b) octahedral sites at $(\frac{1}{2}\frac{1}{2}\frac{1}{2})$, with only a small number of cations in the tetrahedral 8(c) sites at $(\frac{1}{4}\frac{1}{4}\frac{1}{4})$. This is of note because it is very unusual for an ordered silver halide compound to have octahedrally coordinated silver ions, let alone for a disordered superionic phase.
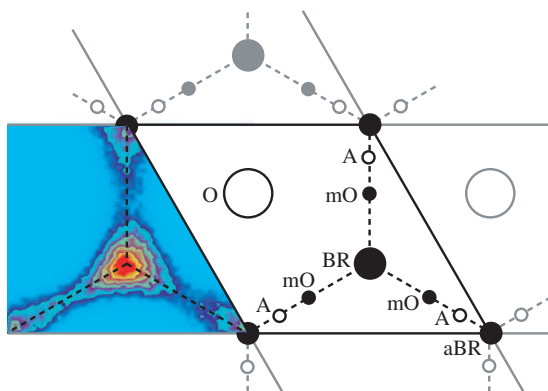
Figure 15. A schematic representation of the two-dimensional conduction layer in β-alumina (after [113]) showing the bridging oxygen positions (large open circles) and a variety of possible locations for the conducting cation, labelled (as in the existing literature) BR—Beevers–Ross; aBR—anti-Beevers–Ross; mO—mid-oxygen; A—A-site. The left-hand side of the figure also shows the average density of cations from a MD simulation of a non-stoichiometric β-alumina at $T = 1500$ K, showing the preference for BR sites and A sites around aBR sites (see [113] for details).

In both the Hg^{2+}- and Pb^{2+}-doped compounds, doping appears to favour the fcc (or hcp) lattice over the bcc lattice (the bcc structure is only observed in ε-Ag_2HgI_4 and then at higher temperatures than for undoped α-AgI). This is presumably because the Hg^{2+} and Pb^{2+} cations can adopt their preferred regular tetrahedral and octahedral coordinations, respectively, within the fcc structure. In contrast, in the bcc lattice the tetrahedral and octahedral sites are distorted. The more surprising result is that the Ag^+ cations also adopt an unusual octahedral environment in fcc $Ag_xPb_{1-x}I_{2-x}$, suggesting that the minority dopant is imposing its favoured coordination on the structure. This is similar to the suggestions about the isovalent cation doping playing a 'determinative structural role' in Ag_4RbI_5; dopants attempt to adopt their higher-coordination environments and, in the process, modify the anion sublattice to increase the degree of face sharing of the anion tetrahedra [108]. As a consequence, the conductivity of Ag_4RbI_5 is also enhanced. This argument does not completely hold for these aliovalent-doped compounds. Doping does enhance the conductivity (the fcc structured doped phases achieve higher ionic conductivities than the related γ-AgI or γ-CuI undoped phases) and the coordination is significantly modified by the Pb^{2+} dopants. However, the resultant doped fcc (or equivalent hcp) structures are retained to higher temperatures and, if compared to the undoped bcc α-AgI structure, actually have fewer face-sharing tetrahedra.

5.3. Alkali metal superionic conductors

This section concerns a number of different types of superionic conductor. The materials in each of the first two sections 5.3.1 and 5.3.2, although they predominantly refer to alkali metal ionic conductors, are considered together because they have a common dimensionality associated with the ionic conduction. The final two sections 5.3.3 and 5.3.4 describe two more families of alkali metal conductors, typified by the high-temperature superionic phase of Li_2SO_4 and those associated with the so-called NASICON acronym.

5.3.1. Two-dimensional superionic conductors. The β- and β''-aluminas typify two-dimensional type III superionic conductors and they have been particularly well studied because
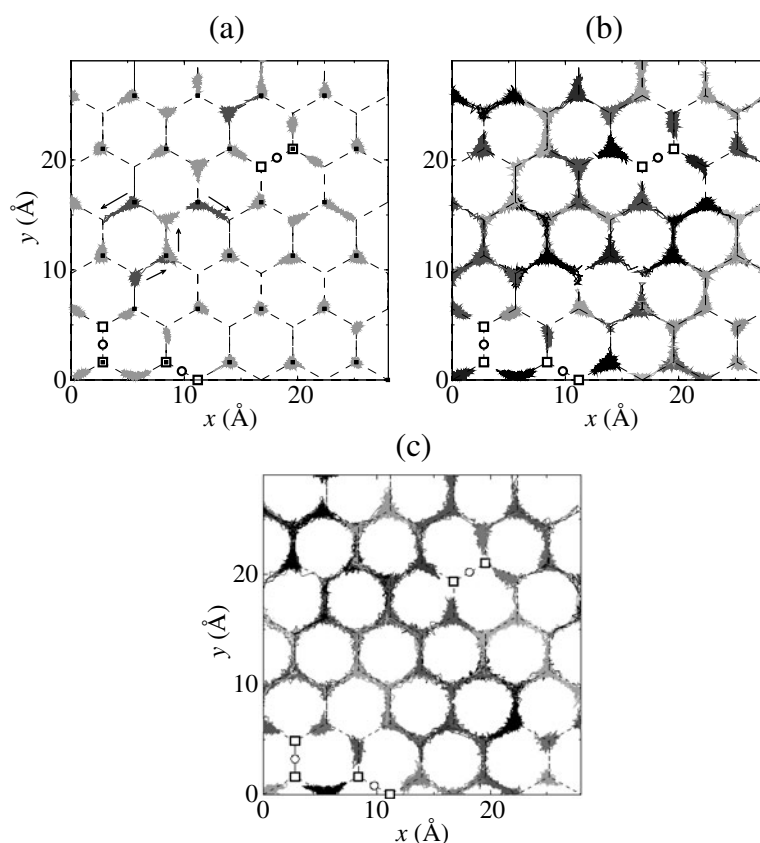
Figure 16. Trajectories of sodium ions in the conduction plane of non-stoichiometric β-alumina during a MD simulation [113]. (a) A 100 ps run at 300 K; (b) 100 ps at 700 K; (c) 50 ps at 1500 K. Open circles and squares denote interstitial oxygens and their neighbouring BR and aBR sites, respectively. Arrows in (a) show a series of correlated jumps. See [113] for further details.

they show high ionic conductivity at room temperature. Their structures are composed of two parts, a thick layer of non-conducting atoms in a spinel arrangement (the 'spinel block') and a loosely packed layer of conducting ions and bridging oxygen atoms forming a two-dimensional hexagonal lattice (the 'conduction plane'); see figure 15. The general formula is $(Al_{11-y}Mg_yO_{16})[M_{1+x+y}O_{1+x/2}]$ where M is the conducting alkali ion and the round and square brackets correspond to the atoms in the spinel block and conduction plane, respectively [109]. The difference between the β- and β''-alumina structures is that in the former the conduction plane lies on a mirror plane and is strictly planar, whereas in the latter the conduction plane is not constrained by symmetry and need not be planar.

The disorder in the two-dimensional conduction plane gives rise to strong diffuse scattering features in x-ray diffraction patterns [110–112]. These have a rod-like form perpendicular to the conduction planes, the intensities of which are modulated due to correlations between the conducting ions and the neighbouring ions in the spinel blocks. More recently, research has concentrated on understanding the conducting ion trajectories (e.g. using MD simulations [113]; figure 16), interpretation of the mixed alkali effect, which gives rise to non-linear behaviour in the conductivity on mixing two types of conducting
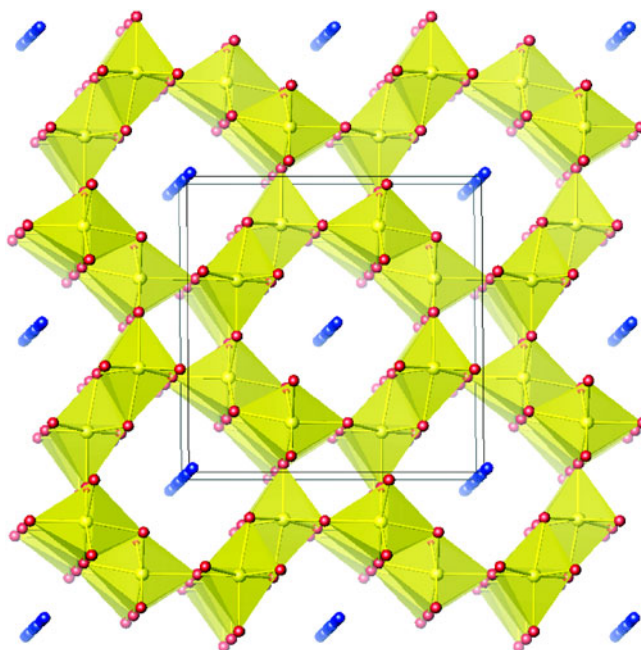
Figure 17. The hollandite structure, showing how the open framework of $(B/C)O_6$ octahedra results in one-dimensional conduction channels parallel to the c-axis.

ion (e.g. using MC simulations [114]) and local probe investigations of structural detail (e.g. XANES investigations of the local environment of the Al ions in the spinel blocks [109]). There have also been studies of the isostructural compound K^+ β-ferrite aiming to understand the structural disorder and magnetism in these compounds (see, for example, [115]).

5.3.2. One-dimensional superionic conductors. Materials with the hollandite structure typify one-dimensional type III superionic conductors. They have received increased interest recently as possible anodes for lithium-ion batteries and because of the importance of α-MnO$_2$, whose structure is related to that of hollandite. The general chemical formula for hollandite is $A_{2x}B_yC_{8-y}O_{16}$ where the charges a, b and c on the A, B and C cations are related by $xa + yb + (8 - y)c = 32$ with $a = 1$ or 2, $b = 1$, 2 or 3 and $c = 4$. The hollandite structure consists of a framework of $(B/C)O_6$ octahedra, connected in such a way as to produce one-dimensional channels which are composed of a linear sequence of larger cavities in the structure (see figure 17). The conducting A cations therefore may move within these channels, which have a periodic variation in width, corresponding to the (wider) cavities and (narrower) connecting regions, sometimes known as 'bottlenecks'. The natural potassium hollandite mineral priderite, $K_{1.54}Mg_{0.77}Ti_{7.23}O_{16}$, typifies the structure and has been much studied [116].

The majority of studies of the structural disorder are therefore concerned with the distribution of the conducting ions within these channels and the possible ordering between them. The characteristic x-ray scattering signature for this would be composed of superlattice reflections (when complete ordering is observed) and/or strong diffuse streaks perpendicular to the tunnel direction (when only partial ordering is observed). Much of the x-ray and electron diffraction work is referenced in [116–118] and describes the interpretation of the scattering in terms of intrachannel and interchannel correlations of the conducting cations. More recently, a series of MD simulations have been used to investigate various aspects of the local arrangements

within hollandite [119], including the composition [120] and temperature [121] dependence. The lattermost study, looking at the behaviour of sodium ions in a chromium titanium hollandite with approximate composition $Na_{1.7}Cr_{1.7}Ti_{6.3}O_{16}$, maps out the distribution of potassium ions within the channels as a function of temperature and assesses the collective nature of the ionic conduction.

5.3.3. Alkali metal sulphates.   The interest in Li_2SO_4 and related materials stems from the role the sulphate groups may or may not play in the mechanism for conduction. The basic structure for the fcc superionic phase has the conducting cations on 8c $(\frac{1}{4}\frac{1}{4}\frac{1}{4})$ sites and the sulphur atom of the SO_4^{2-} anion on 4a (000) sites in space group $Fm\bar{3}m$. The oxygen ions are rotationally disordered about the sulphur ion and this, combined with the highly disordered cation sublattice, results in substantial diffuse scattering and a very small number of observable Bragg reflections (for example, 20 reflections were observed in a single-crystal study [9]). The debate in the literature concerns whether the ionic diffusion is aided by, or independent of, the rotational motion of the SO_4 units (compare [122] with [123]). RMC models have also been produced for superionic Li_2SO_4 and $LiNaSO_4$ from total neutron scattering measurements of powdered samples [124]. They concluded that there was evidence for both types of mechanism. The modelling has recently been extended to investigate the proton conductor, $CsDSO_4$, which shows much stronger correlation between the proton diffusion and sulphate rotation [125].

5.3.4. NASICON and related materials. $NaZr_2(PO_4)_3$ typifies a very broad range of open network structures of general formula $M_xA_2(XO_4)_3$ which are composed of corner-linked octahedral AO_6 and tetrahedral XO_4 units [126]. The term NASICON (Na superionic conductor) was coined with the discovery that $Na_3Zr_2(SiO_4)_2(PO_4)$ possessed particularly high ionic conductivity (0.2 Ω^{-1} cm^{-1} at 573 K) [127, 128]. The term LISICON refers to a similar acronym and is typified by (for example) $Li_{(2+2x)}Zn_{(1-x)}GeO_4$ [129]. Much work was carried out on these materials in the early 1980s (see e.g. articles in [130]), and they remain topical as possible cathode materials for lithium-ion batteries [131]. One of the major difficulties in this field is reproducibility between different samples, since the physical properties are crucially dependent on preparation methods and thermal history of the sample. Furthermore, the samples have a strong tendency to form polytypes, and each family has a large range of possible compositions.

   With this in mind, and as is usual for superionic conductors, the challenge is to identify the locations of, and conducting pathway for, the conducting ions (made harder by the low x-ray scattering from lithium ions). Early x-ray single-crystal diffraction measurements showed that the alkali ions in the average structure possessed very large anisotropic atom displacement parameters [132]. Neutron powder diffraction on $Na_{(1+x)}Zr_2(SiO_4)_x(PO_4)_{(3-x)}$ showed that high ionic conductivities correspond to those compositions whose network structure produced the least constrictive bottlenecks between occupied sodium sites, with the highest conductivity corresponding to $x = 2$ [133, 134]. This is further highlighted at the monoclinic-to-hexagonal phase transition at ~423 K. Here there is a significant increase in conductivity in the high-temperature hexagonal phase, with wider bottlenecks than in the low-temperature structure. It is interesting that these changes in bottleneck size are accomplished with only very small changes in the displacements of the atoms in the network structure.

   Recently there have been a series of high-resolution neutron powder diffraction experiments on various polymorphs of $LiZr_2(PO_4)_3$ [135–137]. Of the four polymorphs studied, α-$LiZr_2(PO_4)_3$ (stable above ~333 K) forms the undistorted rhombohedral NASICON structure. Below ~333 K, α-$LiZr_2(PO_4)_3$ transforms to the triclinic α'-$LiZr_2(PO_4)_3$ phase.

The equivalent β-(monoclinic) and β'-(orthorhombic) phases, with the $Fe_2(SO_4)_3$ structure, have also been studied [137]. Of these, the α-phase has the highest ionic conductivity ($\sigma \sim 10^{-2}\ \Omega^{-1}\ cm^{-1}$ at 573 K, compared with $\sigma \sim 5 \times 10^{-4}\ \Omega^{-1}\ cm^{-1}$ for the β-phase at the same temperature), and the β'-phase has the lowest ($\sigma \sim 10^{-10}\ \Omega^{-1}\ cm^{-1}$ at room temperature, compared with $\sigma \sim 5 \times 10^{-8}\ \Omega^{-1}\ cm^{-1}$ for the α'-phase at the same temperature). However, even within the α-phase there is a large change in conductivity from $\sim 10^{-8}\ \Omega^{-1}\ cm^{-1}$ just above the α'–α phase transition and rising steeply with increased temperature until an order-of-magnitude change at 550 K to a superionic regime occurs [138]. The neutron powder diffraction measurements show that these differences in ionic conductivity are due to the different numbers of sites available to the lithium ions. This view is supported by recent MD simulations [139] which not only show that the high-temperature transition within the α-phase is due to a disordering of Li ions between two distinct sites, but also identifies a possible conduction pathway via an additional site midway between the two sites. This is also consistent with the proposed conduction mechanism in $Na_3Sc_2(PO_4)_3$ [140]. Pathways in the general NASICON framework have also been investigated using bond valence mismatches [141]. Most probable pathways are identified according to those that have the lowest bond valence mismatch, and the highest value of bond valence along these pathways is related to the ionic conductivity and the angles within the network structure. Hence the structure within any given series of NASICON materials could be used to predict the expected ionic conductivity. To date, though, there have not been any structural investigations of these materials using diffuse scattering, presumably because of their structural complexity and difficulties in consistent sample preparation.

It is also interesting to note that zirconia-deficient stoichiometries such as $Na_{(1+x)}Zr_{(2-x/3)}Si_xP_{(3-x)}O_{(12-2x/3)}$ (or $Na_{(1+x)}Zr_2(SiO_4)_x(PO_4)_{(3-x)}$–$(ZrO_2)_{x/3}$) having $0 \leqslant x \leqslant 3$ produce a related glassy material, termed NASIGLAS, which has high ionic conductivity for a range of compositions, $1.6 \leqslant x \leqslant 3$ (see for example [142] and references therein).

5.4. Amorphous superionic conductors

Understanding the superionic process within an amorphous structure has proved a particular challenge. The fundamental problem is how to extract detailed structural information from aperiodic multi-component materials from total scattering data. Most of the recent advances have therefore evolved from neutron isotopic substitution experiments and the development of the RMC method which, when sensibly applied, can extract structural information from limited data. X-ray spectroscopic techniques, such as EXAFS, have also played an important part, since they can probe the local environment of dopant atoms.

The total scattering measurement from an n-component material is composed of a weighted sum of $\frac{1}{2}n(n+1)$ partial structure factors (see [35]). In favourable circumstances, measurements of a series of chemically identical samples with different isotopes can be used to separate the contributions from the different partial structure factors (see the work on Ag_2Se, section 5.2.4). However, for even the chemically simple superionic glasses, such as $AgPS_3$ [143], six distinct isotopic substitution neutron total scattering measurements would be needed for a complete separation. This is rarely possible in practice, since isotopes with significantly different neutron scattering lengths only exist in large enough quantities for a small number of elements. Fortunately silver and copper do have suitable isotopes (^{107}Ag ($b = 7.505$ fm) and ^{109}Ag ($b = 4.21$ fm), ^{63}Cu ($b = 6.4$ fm) and ^{65}Cu ($b = 10.6$ fm), respectively) and, since silver and copper are frequently the conducting ion in superionic glasses, some progress may be made.

In [143], three separate neutron total scattering measurements of $AgPS_3$ were made, using $^{107}AgPS_3$, $^{N}AgPS_3$ and $^{109}AgPS_3$ samples (where ^{N} signifies the natural isotopic abundance).

A second-order difference method [144] was then used to extract three sets of correlation functions, $A_{Ag-Ag}(Q)$, the partial structure factor for Ag–Ag correlations, and two sets of composite functions, $\Delta_{Ag-P/S}(Q)$ and $\Delta_{P/S-P/S}(Q)$, which contain Ag–P/S and P/S–P/S correlations, respectively. There is a degree of overdetermination in this method (e.g. the three $\Delta_{Ag-P/S}(Q)$ are related by a known scale factor) and this can be used to check the reliability of the separation. The Fourier transforms of the above functions were then used to investigate the nature of the ionic conduction and the relationship between glassy $AgPS_3$ and crystalline analogues. It was concluded that the local structure of the glass was significantly different from that of the corresponding crystal and that the silver ions were widely distributed within the glassy matrix over a large number of sites.

There have been a number of other similar studies using neutron total scattering with isotopic substitution. These include $([Ag,Cu]_2Se)_{0.25}(AsSe)_{0.75}$ [144]; $(Ag_2S)_x(GeS_2)_{1-x}$, with $x = 0.3$, 0.4 and 0.5 [145, 146]; $(Li_2S)_{0.5}(SiS_2)_{0.5}$ using ^NLi and ^6Li which have negative and positive neutron scattering lengths, respectively [147]; $(Ag_2Te)_{0.5}(As_2Te_3)_{0.5}$ [148]; and $(CuI)_{0.6}(Sb_2Se_3)_{0.4}$ [149]. The initial work on $(Ag_2S)_{0.5}(GeS_2)_{0.5}$ [145] additionally used RMC modelling to generate three-dimensional models of the structure from $(^NAg_2S)_{0.5}(GeS_2)_{0.5}$ and compared the results with those from the isotopically enriched samples.

RMC modelling has been used extensively on another superionic glassy system, $(AgI)_x(AgPO_3)_{1-x}$ [150, 151]. Here, instead of using isotopic substitution methods to separate the different pair correlation functions, the three-dimensional RMC models are constructed on the basis of a variety of structural information. Neutron and x-ray total scattering, together with Ag K-edge and I L_{III}-edge EXAFS, were carried out on samples with seven different compositions between $x = 0$ and 0.5. A three-dimensional structural model was initially created of chains of PO_4 tetrahedra, each having two bridging and two non-bridging oxygen atoms. The PO_4 chain structure was then interspersed with Ag and I atoms to give the required chemical composition and overall density. This structure was then refined with RMC modelling using the four measured data sets and whilst maintaining the initial P–O bonding. The agreement is shown in figure 18. Extremely good fits were obtained to the neutron and x-ray total scattering data and reasonable fits to the EXAFS patterns.

Two important conclusions were reached. First, the so-called first sharp diffraction peak (FSDP) which occurs at $Q \sim 0.7$ Å^{-1} is more pronounced in the neutron diffraction pattern than in the x-ray diffraction. The neutron FSDP had been ascribed earlier to AgI clusters in the glass (e.g. [152]). However, since the x-ray diffraction is dominated by Ag and I scattering and the FSDP in the x-ray pattern is small, it is more likely that the FSDP arises from intermediate-range order of the PO_4 chains. In particular, it was found that the reduction of the chain density, as the AgI dopant concentration increases, is the most significant contribution to the increase in intensity of the FSDP. (The FSDP has been investigated in greater detail recently for a number of superionic glasses using neutron total scattering, small-angle neutron scattering and RMC modelling [153].) Secondly, the three-dimensional structural models are analysed to determine a structural basis for the ionic conductivity. By investigating the free volume in the model available to the silver ions, conducting pathways within the model were mapped out. A percolation transition was observed at around $x = 0.3$; below $x = 0.3$, the silver ions exist in small non-connecting pathways; above $x = 0.3$ the model has one fully connected pathway containing the majority of silver ions. This is consistent with the observed ionic conductivity, which increases with increasing AgI dopant. The results are summarized qualitatively by the concept of a 'modified random network' [154] whereby a continuous random 'network' glass structure is modified by the introduction of additional AgI 'salt' dopant. At low AgI concentrations, the silver ions largely bond with the non-bridging oxygen atoms in the PO_4 network and the structure is maintained. As the AgI concentration increases, the PO_4 chains
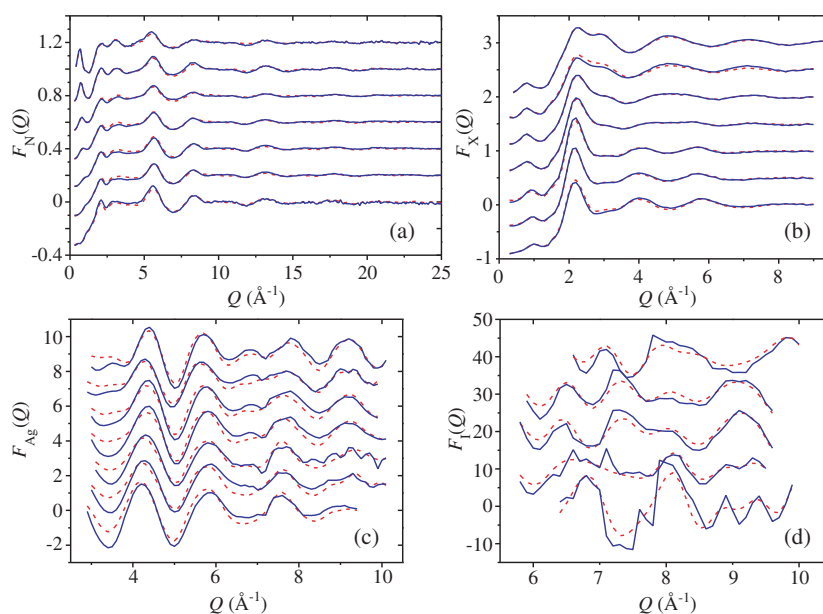
Figure 18. Experimental structure factors (full curve) and RMC fits (dashed curve) for $(AgI)_x(AgPO_3)_{1-x}$ superionic glasses. (a) Neutron diffraction, (b) x-ray diffraction and (c) Ag K-edge EXAFS with $x = 0.0, 0.05, 0.1, 0.2, 0.3, 0.4$ and 0.5. (d) I L_{III}-edge EXAFS with $x = 0.1, 0.2, 0.3, 0.4$ and 0.5. (Compositions as listed are plotted bottom to top and offset for clarity [151].)

are forced further apart, the conductivity increases, but the connectivity eventually breaks and the glass crystallizes. This free volume argument for ionic conductivity in amorphous materials has been broadened to include other systems and discussed in greater detail in a later work [155].

RMC models have also been used in conjunction with bond valence summations for many superionic glasses with mobile silver ions, including $(AgI)_{0.75}(Ag_2MO_4)_{0.25}$, with M $=$ W and Mo; $(AgI)_{0.6}(Ag_xO–xB_2O_3)_{0.4}$, with $x = 1$ and 2; $(AgI)_x(AgPO_3)_{1-x}$ with $x = 0, 0.1$, 0.3 and 0.5; the low-conducting $Ag_2O–nB_2O_3$ with $n = 2$ and 4 [16, 17]. Here, the RMC modelling includes an additional 'soft constraint' to restrict the silver ions to locations within the models with suitable bond valences, thus yielding chemically reasonable structural models in good agreement with the available structural data. The RMC-generated models are then analysed to determine the bond valence sum mismatch for a hypothetical silver ion placed in small volume elements throughout the volume of the models. Those volume elements whose mismatch was below a certain value were considered accessible to silver ions and hence could form part of a conduction pathway. Figure 19 shows a section of an RMC-generated configuration of amorphous $(AgI)_{0.6}(Ag_2O–2B_2O_3)_{0.4}$, together with a silver-ion bond valence isosurface calculated from the atom positions in the configuration. If a pathway extends across the model, then, through periodic boundary conditions, it can contribute to long-range ionic conduction. The volume fraction, F, of these conduction pathways is related to the experimental dc conductivity, σ, via the relationship $\log(\sigma T) \propto \sqrt[3]{F}$. The pathway volume fraction is distinct from the free volume fraction, since, for example, the bond valence sum mismatch would only include the edges of large voids within the structure. It is therefore a refinement of the earlier free volume analysis [150] and should be more representative of
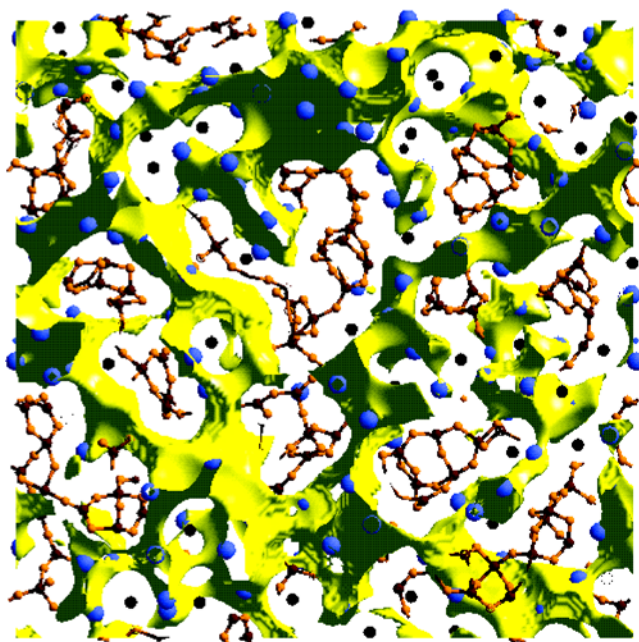
Figure 19. A 5 Å thick section through an RMC-generated model of $(AgI)_{0.6}$–$(Ag_2O$–$2B_2O_3)_{0.4}$ superionic glass [50]. Superimposed on the model is an isosurface corresponding to the likely conduction pathway for silver ions, as determined from a bond valence mismatch calculation [16]. Ag^+ and I^- are shown as large grey and black spheres, respectively. The borate network is shown as a joined sequence of B (small dark grey spheres) and O (small light grey spheres).

the volume available to the conducting ions. Random walk simulations through the bond valence-generated conduction pathways were also used to relate the self-diffusion constant to the experimental ionic conductivity.

The superionic borate glasses, such as $(AgI)_x(Ag_2O$–$nB_2O_3)_{1-x}$, have also been much studied using x-ray diffraction and EXAFS [156, 157]. The addition of the network modifier, Ag_2O, to the network former, B_2O_3, strongly changes the local and intermediate-range order of the glass from a planar triangular structure to a structure which also contains negatively charged BO_4 units. This gives rise to an ionic conductivity, which is enhanced further by the addition of the dopant salt, AgI, such that values typical of superionic conductors are observed at room temperature. The AgI dopant has the effect of expanding the borate glassy network, without significantly changing the network structure. Again, evidence for clusters of 'crystalline' AgI were not found in the glass.

This may be contrasted with a number of studies of specially prepared glassy samples where microcrystallites of α-AgI are formed within the glassy matrix. The initial paper [158] described how AgI–Ag_3BO_3 mixtures were melted and then cooled extremely quickly using twin-roller quenching. Compositions with around 90 mol% AgI, cooled to room temperature at $\sim 5 \times 10^5$ K s^{-1} or faster, produced a glassy matrix containing crystallites of the high-temperature α-AgI superionic phase. The samples had a high ionic conductivity at room temperature ($\sigma \sim 0.1$ Ω^{-1} cm^{-1}), a small increase at 420 K (the β–α phase transition for bulk crystalline AgI) due to the conversion of a small amount of residual β-phase and, on cooling, the α-AgI crystallites transformed to β-AgI at around 383 K. Other similar materials have also been identified, in the family AgI–Ag_2O–M_xO_y, with M_xO_y = B_2O_3, GeO_2, P_2O_5, V_2O_5,

MoO_3 and WO_3 [156, 160]. Since the early papers, there has been considerable work (using x-ray diffraction, differential scanning calorimetry, field emission scanning electron microscopy and NMR) on a variety of related glassy materials. These measurements have investigated the influence of composition, cooling rates and repeated heat cycling on the relative formation of amorphous and crystalline (β- and α-AgI) components (e.g. [161–163]).

5.5. Other superionic systems

There are a number of other superionic systems that have been studied. These include proton conductors (e.g. [125, 164]), polymer electrolytes (e.g. [165]) and superionic materials prepared as thin films or nanocrystals (e.g. [166]). However, with the exception of the proton conductors (which is a complete scientific area in its own right), there have not been many rigorous investigations of the structural disorder associated with the superionic process. In the main, therefore, they are emergent systems and it would be pre-emptive to summarize them here.

6. Conclusions

This review provides a detailed summary of the current state of investigation of the disordering processes in superionic conductors. These span from the extensive work on typical systems such as α-AgI and α-CuI, which are amenable to many different investigative methods, to the more technologically relevant, but chemically more complex systems, where the disorder associated with superionic conduction is less easy to characterize. In general, since the interest concerns the nature of the structural disorder resulting from, or contributing to, a dynamic process, it is a difficult area to characterize. Often the most progress is made when different complementary methods are combined. This is seen in the MD and RMC studies of CuI, or the combined neutron isotopic substitution, x-ray diffraction and EXAFS measurements of superionic glasses. Also, recent investigations at high pressure and high temperature may be seen as an important alternative to chemical doping studies. As this review shows (by deliberately focusing on current work), superionic conductor research is still active; largely driven by the need to underpin various technological advances. It is believed that this will continue and further improvements in our understanding of the superionic state will evolve in the years to come.

References

[1] Boyce J B and Huberman B A 1979 *Phys. Rep.* **51** 189
[2] Funke K 1976 *Prog. Solid State Chem.* **11** 345
[3] Chandra S 1981 *Superionic Solids* (Amsterdam: North-Holland)
[4] Andersen N H, Clausen K N and Kjems J K 1986 Fast ion conductors *Neutron Scattering and Condensed Matter Research (A Volume in the 'Methods of Experimental Physics' Series)* ed K Sköld and D L Price (New York: Academic)
[5] Keen D A and Hull S 1995 *J. Phys.: Condens. Matter* **7** 5793
[6] Sinclair W, McLaughlin G M and Ringwood A E 1980 *Acta Crystallogr.* B **36** 2913
[7] Yoshiasa L, Koto K, Kanamaru F, Emura S and Horiuchi H 1987 *Acta Crystallogr.* B **43** 434
[8] Nilsson L, Thomas J O and Tofield B C 1980 *J. Phys. C: Solid State Phys.* **13** 6441
[9] Andersen N H, Banaranayake P W S K, Careem M A, Dissanayake M A K L, Wijayasekera C N, Kaber R, Lundén A, Mellander B-E, Nilsson L and Thomas J O 1992 *Solid State Ion.* **57** 203
[10] Hull S, Keen D A, Sivia D S and Berastegui P 2002 *J. Solid State Chem.* **165** 363
[11] Sivia D S and David W I F 2001 *J. Phys. Chem. Solids* **62** 2119
[12] Brese N E and O'Keeffe M 1991 *Acta Crystallogr.* B **47** 192

[13] Swenson J and Adams St 2001 *Phys. Rev.* B **64** 024204
[14] Brown I D and Altermatt D 1985 *Acta Crystallogr.* B **41** 244
[15] Adams St 2001 *Acta Crystallogr.* B **57** 278
[16] Adams St and Swenson J 2000 *Phys. Rev.* B **63** 054201
[17] Adams St 2000 *Solid State Ion.* **136/137** 1351
[18] Keen D A, Hull S, Hayes W and Gardner N J G 1996 *Phys. Rev. Lett.* **77** 4914
[19] Nield V M and Keen D A 2001 *Diffuse Neutron Scattering From Crystalline Materials* (Oxford: Oxford University Press)
[20] Currat R and Pynn R 1979 Neutron scattering *Treatise on Materials Science and Technology* vol 15, ed G Kostorz (New York: Academic) pp 131–89
[21] Schweika W 1990 *Mater. Res. Soc. Symp. Proc.* **166** 249
[22] Hutchings M T, Clausen K N, Dickens M H, Hayes W, Kjems J K, Schnabel P G and Smith C 1984 *J. Phys. C: Solid State Phys.* **17** 3903
[23] Kjems J K, Andersen N H and Schoonman J 1983 *Physica* B **120** 357
[24] Goff J P, Hayes W, Hull S, Hutchings M T and Clausen K N 1999 *Phys. Rev.* B **59** 14 202
[25] Neder R B, Frey F and Schulz H 1990 *Acta Crystallogr.* A **46** 792
[26] Lonsdale K and Smith H 1941 *Proc. R. Soc.* A **179** 8
[27] Frey F 1995 *Acta Crystallogr.* B **51** 592
[28] Butler B D, Haeffner D R, Lee P L and Welberry T R 2000 *J. Appl. Crystallogr.* **33** 1046
     Butler B D, Haeffner D R, Lee P L and Welberry T R 2000 *J. Appl. Crystallogr.* **33** 1449
[29] Estermann M A and Steurer W 1998 *Phase Transit.* **67** 165
[30] Osborn J C and Welberry T R 1990 *J. Appl. Crystallogr.* **23** 476
[31] Proffen T, Neder R B and Frey F 1996 *J. Solid State Chem.* **126** 33
[32] Keen D A, Wilson C C and Gutmann M J 2002 private communication
[33] Howe M A, McGreevy R L and Howells W S 1989 *J. Phys.: Condens. Matter* **1** 3433
[34] Hannon A C, Howells W S and Soper A K 1990 *Inst. Phys. Conf. Ser.* **107** 193
[35] Keen D A 2001 *J. Appl. Crystallogr.* **34** 172
[36] Barnes A C, Hamilton M A, Beck U and Fischer H E 2000 *J. Phys.: Condens. Matter* **12** 7311
[37] Filipponi A 2001 *J. Phys.: Condens. Matter* **13** R23
[38] Rehr J J and Albers R C 2000 *Rev. Mod. Phys.* **72** 621
[39] Boyce J B, Hayes T M and Mikkelsen J C 1981 *Phys. Rev.* B **23** 2876
[40] Hayes T M, Boyce J B and Beeby J L 1978 *J. Phys. C: Solid State Phys.* **11** 2931
[41] Hayes T M and Boyce J B 1980 *J. Phys. C: Solid State Phys.* **13** L731
[42] Allen M P and Tildesley D J 1987 *Computer Simulation of Liquids* (Oxford: Oxford University Press)
[43] Gillan M J 1989 *Ionic Solids at High Temperatures* ed A M Stoneham (Singapore: World Scientific) p 169
[44] Vashishta P and Rahman A 1978 *Phys. Rev. Lett.* **40** 1337
[45] Parrinello A, Rahman A and Vashishta P 1983 *Phys. Rev. Lett.* **50** 1073
[46] Tallon J L 1988 *Phys. Rev.* B **38** 9069
[47] Metropolis N, Rosenbluth A W, Rosenbluth M N, Teller A H and Teller E 1953 *J. Phys. Chem.* **21** 1087
[48] Keen D A, Hayes W and McGreevy R L 1990 *J. Phys.: Condens. Matter* **2** 2773
[49] McGreevy R L and Pusztai L 1988 *Mol. Simul.* **1** 359
[50] McGreevy R L 2001 *J. Phys.: Condens. Matter* **13** R877
[51] Tucker M G, Dove M T and Keen D A 2001 *J. Appl. Crystallogr.* **34** 630
[52] Hutchings M T 1987 *J. Chem. Soc. Faraday Trans.* **83** 1083
[53] Clausen K N, Hackett M A, Hayes W, Hull S, Hutchings M T, MacDonanld J E, McEwan K A, Osborn R and Steigenberger U 1989 *Physica* B **156–7** 103
[54] Hayes W and Hutchings M T 1989 *Ionic Solids at High Temperatures* ed A M Stoneham (Singapore: World Scientific) p 247
[55] Hofmann M, Hull S, McIntyre G J and Wilson C C 1997 *J. Phys.: Condens. Matter* **9** 845
[56] Proffen T, Neder R B and Frey F 1996 *Acta Crystallogr.* B **52** 59
[57] Hull S and Wilson C C 1992 *J. Solid State Chem.* **100** 101
[58] Welberry T R, Withers R L, Thompson J G and Butler B D 1992 *J. Solid State Chem.* **100** 71
[59] Hayakawa M, Bardham P and Cohen J B 1975 *J. Appl. Crystallogr.* **8** 87
[60] Welberry T R and Butler B D 1995 *Chem. Rev.* **95** 2369
[61] Welberry T R, Butler B D, Thompson J G and Withers R L 1993 *J. Solid State Chem.* **106** 461
[62] Welberry T R, Withers R L and Mayo S C 1995 *J. Solid State Chem.* **115** 43
[63] Welberry T R and Proffen Th 1998 *J. Appl. Crystallogr.* **31** 309
[64] Proffen Th and Welberry T R 1998 *J. Appl. Crystallogr.* **31** 318

[65] Villella P, Conradson S D, Espinosa-Faller F J, Foltyn S R, Sickafus K E, Caldez J A and Degueldre C A 2001 *Phys. Rev.* B **64** 104101
[66] Nield V M and Hayes W 1995 *Defect Diffus. Forum* **125–6** 37
[67] Nield V M, Keen D A, McGreevy R L and Hayes W 1993 *Solid State Ion.* **66** 247
[68] Tsuchiya Y, Tamaki S and Waseda Y 1979 *J. Phys. C: Solid State Phys.* **12** 5361
[69] Cava R J, Fleming R M and Rietman E A 1983 *Solid State Ion.* **9–10** 1347
[70] Sakuma T and Hoshino S 1993 *J. Phys. Soc. Japan* **62** 2048
[71] Dalba G, Fornasini P, Gotta R, Cozzini S, Ronchetti M and Rocca F 1994 *Solid State Ion.* **69** 13
[72] Montani R A 1992 *J. Phys. Chem. Solids* **53** 1211
[73] Hull S and Keen D A 1996 *J. Phys.: Condens. Matter* **8** 6191
[74] Hull S, Keen D A, Hayes W and Gardner N J G 1998 *J. Phys.: Condens. Matter* **10** 10 941
[75] Nield V M, McGreevy R L, Keen D A and Hayes W 1994 *Physica* B **202** 159
[76] Chahid A and McGreevy R L 1998 *J. Phys.: Condens. Matter* **10** 2597
[77] Zheng-Johansson J X M and McGreevy R L 1996 *Solid State Ion.* **83** 35
[78] Keen D A and Hull S 1995 *J. Phys.: Condens. Matter* **7** 5793
[79] Ihata H and Okazaki H 1997 *J. Phys.: Condens. Matter* **9** 1477
[80] Hull S and Keen D A 1994 *Phys. Rev.* B **50** 5868
[81] Hofmann M, Hull S and Keen D A 1995 *Phys. Rev.* B **51** 12 022
[82] Rino J P, Hornos Y M M, Antonio G A, Ebbsjö I, Kalia R K and Vashishta P 1988 *J. Chem. Phys.* **89** 7542
[83] Keen D A and Hull S 1998 *J. Phys.: Condens. Matter* **10** 8217
[84] Hamilton M 2000 *PhD Thesis* University of Bristol, UK
[85] Keen D A, Hayes W and McGreevy R L 1990 *J. Phys.: Condens. Matter* **2** 2773
[86] Hamilton J F 1988 *Adv. Phys.* **37** 359
[87] Nield V M, Keen D A, Hayes W and McGreevy R L 1992 *J. Phys.: Condens. Matter* **4** 6703
[88] Maier J 1996 *Solid State Ion.* **86–8** 55
[89] DiCicco A, Taglienti M, Minicucci M and Filipponi A 2000 *Phys. Rev.* B **62** 12 001
[90] Tasseven C, Trullàs J, Alcaraz M, Silbert M and Giró A 1997 *J. Chem. Phys.* **106** 7286
[91] Keen D A, Hull S, Hayes W and Gardner N J G 1996 *Phys. Rev. Lett.* **77** 4914
[92] Mellander B-E 1982 *Phys. Rev.* B **26** 5886
[93] Andreoni W and Tosi M P 1983 *Solid State Ion.* **11** 49
[94] Hainovsky N and Maier J 1995 *Phys. Rev.* B **51** 15 789
[95] Hull S, Keen D A, Sivia D S, Madden P A and Wilson M 2002 *J. Phys.: Condens. Matter* **14** L9
[96] Cava R J and McWhan D B 1980 *Phys. Rev. Lett.* **45** 2046
[97] Grier B H, Shapiro S M and Cava R J 1984 *Phys. Rev.* B **29** 3810
[98] Kirchhoff F, Holender J M and Gillan M J 1996 *Phys. Rev.* B **54** 190
[99] Barnes A C, Lague S B, Salmon P S and Fischer H E 1997 *J. Phys.: Condens. Matter* **9** 6159
[100] Ebbsjö I, Vashishta P, Dejus R and Sköld K 1987 *J. Phys. C: Solid State Phys.* **20** L441
[101] Hull S, Keen D A, Gardner N J G and Hayes W 2001 *J. Phys.: Condens. Matter* **13** 2295
[102] Chiodelli G, Magistris A and Schiraldi A 1979 *Z. Phys. Chem., NF* **118** 177
[103] Keen D A and Hull S 2001 *J. Phys.: Condens. Matter* **13** L343
[104] Hoshino S, Sakuma T and Fujii Y 1979 *J. Phys. Soc. Japan* **47** 1252
[105] Hull S and Keen D A 2000 *J. Phys.: Condens. Matter* **12** 3751
[106] Hull S and Keen D A 2000 *J. Phys.: Condens. Matter* **13** 5597
[107] Hull S, Keen D A and Berastegui P 2002 *Solid State Ion.* **147** 97
[108] Chandra S 1981 *Superionic Solids. Principles and Applications* (Amsterdam: North-Holland)
[109] Marcelli A, Mottana A and Cibin G 2000 *J. Appl. Crystallogr.* **33** 234
[110] Cava R J, Reidinger F and Wuensch B J 1981 *Solid State Ion.* **5** 501
[111] Collin G, Boilot J P, Colomban P and Comes R 1986 *Phys. Rev.* B **34** 5838
[112] Kjaer K, Hayes W and Schonfeld B 1987 *J. Phys. C: Solid State Phys.* **20** 6089
[113] Beckers J V L, van der Bent K J and de Leeuw S W 2000 *Solid State Ion.* **133** 217
[114] Meyer M, Maass P and Bunde A 1998 *J. Chem. Phys.* **109** 2316
[115] Edström K, Ito S and Delaplane R G 2000 *J. Magn. Magn. Mater.* **212** 347
[116] Welberry T R and Butler B D 1995 *Chem. Rev.* **95** 2369
[117] Frey F 1997 *Eur. J. Mineral.* **9** 693
[118] Wu X-Z, Fujiki Y, Ishigame M and Horiuchi S 1991 *Acta Crystallogr.* A **47** 405
[119] Michiue Y and Watanabe M 1999 *Phys. Rev.* B **59** 11 298
[120] Michiue Y and Watanabe M 2001 *J. Phys. Soc. Japan* **70** 1986
[121] Michiue Y and Watanabe M 2001 *J. Mater. Chem.* **11** 3103

[122] Nilsson L, Andersen N H and Lundén A 1989 *Solid State Ion.* **34** 111
[123] Secco E A 1993 *Solid State Ion.* **60** 233
[124] Karlsson L and McGreevy R L 1995 *Solid State Ion.* **76** 301
[125] Belushkin A V, Koslenko D P, McGreevy R L, Savenko B N and Zetterström P 1999 *Physica* B **269** 297
[126] Alamo J 1993 *Solid State Ion.* **63–5** 547
[127] Hong H Y-P 1976 *Mater. Res. Bull.* **11** 173
[128] Goodenough J B, Hong H Y-P and Kafalas J A 1976 *Mater. Res. Bull.* **11** 203
[129] Abrahams I, Bruce P G, David W I F and West A R 1989 *Acta Crystallogr.* B **45** 457
[130] *Proc. 4th Int. Conf. on Solid State Ionics (Grenoble, France 1983); Solid State Ion.* **9–10** 793–902
[131] Cushing B L and Goodenough J B 2001 *J. Solid State Chem.* **162** 176
[132] Kohler H and Schulz 1983 *Solid State Ion.* **9–10** 795
[133] Baur W H, Dygas J R, Whitmore D H and Faber J 1986 *Solid State Ion.* **18–19** 935
[134] Didisheim J-J, Prince E and Wuensch B J 1986 *Solid State Ion.* **18–19** 944
[135] Catti M, Stramare S and Ibberson R 1999 *Solid State Ion.* **123** 173
[136] Catti M and Stramare S 2000 *Solid State Ion.* **136–7** 489
[137] Catti M, Morgante N and Ibberson R M 2000 *J. Solid State Chem.* **152** 340
[138] Petit D, Colomban Ph, Collin G and Boilot J P 1986 *Mater. Res. Bull.* **21** 365
[139] Padma Kumar P and Yashonath S 2001 *J. Phys. Chem.* B **105** 6785
[140] Susman S, Delbecq C J and Brun T O 1983 *Solid State Ion.* **9–10** 839
[141] Mazza D 2001 *J. Solid State Chem.* **156** 154
[142] Niyompan A and Holland D 2001 *J. Non-Cryst. Solids* **293–5** 709
[143] Salmon P S, Xin S and Fischer H E 1998 *Phys. Rev.* B **58** 6115
[144] Benmore C J and Salmon P S 1994 *Phys. Rev. Lett.* **73** 264
[145] Lee J H, Owens A P and Elliott S R 1993 *J. Non-Cryst. Solids* **164–6** 139
[146] Lee J H, Owens A P, Pradel A, Hannon A C, Ribes M and Elliott S R 1996 *Phys. Rev.* B **54** 3895
[147] Lee J H, Pradel A, Taillades G, Ribes M and Elliott S R 1997 *Phys. Rev.* B **56** 10 934
[148] Liu J and Salmon P S 1997 *Europhys. Lett.* **39** 521
[149] Salmon P S and Xin S 2002 *Phys. Rev.* B **65** 064202
[150] Wicks J D, Börjesson L, Bushnell-Wye G, Howells W S and McGreevy R L 1995 *Phys. Rev. Lett.* **74** 726
[151] Wicks J D and McGreevy R L 1995 *J. Non-Cryst. Solids* **192+193** 23
[152] Rousselot C, Tachez M, Malugani J P, Mercier R and Chieux P 1991 *Solid State Ion.* **44** 151
[153] Swenson J, Karlsson C, Börjesson L and Heenan R K 2001 *Phys. Rev.* B **64** 134201
[154] Greaves G N 1985 *J. Non-Cryst. Solids* **71** 203
[155] Swenson J, McGreevy R L, Börjesson L and Wicks J D 1998 *Solid State Ion.* **105** 55
[156] Rocca F, Dalba G, Fornasini P and Monti F 1997 *Proc. 2nd Int. Conf. on Borates, Glasses and Melts*
        ed A C Wright, S A Feller and A C Hannon (Sheffield: Society for Glass Technology) p 295
[157] Červinka L, Bergerová J, Dalmaso A and Rocca F 1998 *J. Non-Cryst. Solids* **232–4** 627
[158] Tatsumisago M, Shinkuma Y and Minami T 1991 *Nature* **354** 217
[159] Tatsumisago M, Taniguchi A and Minami T 1993 *J. Am. Ceram. Soc.* **76** 235
[160] Saito T, Tatsumisago M and Minami T 1993 *Solid State Ion.* **61** 285
[161] Tatsumisago M, Okuda K, Itakura N and Minami T 1999 *Solid State Ion.* **121** 193
[162] Kuwata N, Kawamura J, Nakamura Y, Okuda K, Tatsumisago M and Minami T 2000 *Solid State Ion.* **136–7**
        1061
[163] Tatsumisago M, Saito T and Minami T 2001 *J. Non-Cryst. Solids* **293–5** 10
[164] Feki H, Khemakhem H and Abid Y 2001 *J. Phys.: Condens. Matter* **13** 8509
[165] Sun X-G, Xu W, Zhang S-S and Angell C A 2001 *J. Phys.: Condens. Matter* **13** 8235
[166] Lee W, Yoo H I and Lee J K 2001 *Chem. Commun.* 2530